UNIVERSIDAD DE INVESTIGACIÓN DE TECNOLOGÍA EXPERIMENTAL YACHAY

Escuela de Ciencias Físicas y Nanotecnología

TÍTULO: First principles studies of topological defective graphene-based superlattices with H adatoms and C vacancies

Trabajo de integración curricular presentado como requisito para la obtención del título de Físico

Autor:

Leonel A. Cabrera

Tutor:

Henry P. Pinto, Ph.D

Urcuquí, abril 2024

AUTORÍA

Yo, **Cabrera Loor Leonel Angel**, con cédula de identidad 2300237357, declaro que las ideas, juicios, valoraciones, interpretaciones, consultas bibliográficas, definiciones y conceptualizaciones expuestas en el presente trabajo; así cómo, los procedimientos y herramientas utilizadas en la investigación, son de absoluta responsabilidad de el/la autora (a) del trabajo de integración curricular. Así mismo, me acojo a los reglamentos internos de la Universidad de Investigación de Tecnología Experimental Yachay.

Urcuquí, abril 2024

Leonel Angel Cabrera Loor
CI: 2300237357

AUTORIZACIÓN DE PUBLICACIÓN

Yo, **Cabrera Loor Leonel Angel**, con cédula de identidad 2300237357, cedo a la Universidad de Investigación de Tecnología Experimental Yachay, los derechos de publicación de la presente obra, sin que deba haber un reconocimiento económico por este concepto. Declaro además que el texto del presente trabajo de titulación no podrá ser cedido a ninguna empresa editorial para su publicación u otros fines, sin contar previamente con la autorización escrita de la Universidad.

Asimismo, autorizo a la Universidad que realice la digitalización y publicación de este trabajo de integración curricular en el repositorio virtual, de conformidad a lo dispuesto en el Art. 144 de la Ley Orgánica de Educación Superior.

Urcuquí, abril 2024

Leonel Angel Cabrera Loor
CI: 2300237357

Dedicatoria

Para mis padres:
Leonel y Mercedes
Y papitos:
Adriana, Angel, Edilma, y Guido.
«Si he logrado ver más lejos ha sido porque he subido a hombros de gigantes»
-Isaac Newton
Ustedes son los gigantes en mi vida.

Leonel A. Cabrera

Acknowledgements

I extend my gratitude to my lovely family and friends for their support throughout my academic journey, inspiring me to pursue my dreams relentlessly.

Thank you to Diana Ramos, who has been my travel partner during our academic process. Your presence always makes everything more beautiful.

I am particularly grateful to Professor Henry Pinto for introducing me to the quantum realm of solid-state physics and for welcoming me into his research group, CompNano. Your guidance and advice over the years have been invaluable.

I also wish to express my sincere thanks to Domenica Garzon for her explanations and fruitful discussions related to this work.

Finally, I would like to acknowledge the generous support of the School of Physical Sciences and Nanotechnology at Yachay Tech University, and the computing time provided by the TASK Supercomputer Center in Gdansk, Poland, which has been instrumental in my research.

Leonel A. Cabrera

Resumen

El grafeno es conocido por sus excepcionales atributos electrónicos y estructurales. Sin embargo, su aplicabilidad en nanoelectrónica y aplicaciones magnéticas está limitada por la ausencia de una banda prohibida y características magnéticas. Dado que los estudios experimentales pueden ser costosos y llevar mucho tiempo, es esencial explorar el impacto de los defectos en las propiedades del grafeno a través de simulaciones. Esta tesis presenta una exploración computacional de superredes de grafeno con defectos topológicos, enfocándose específicamente en los efectos de los adatomos de hidrógeno (H) y las vacantes de carbono (C) en presencia de un defecto en forma de flor (FLD). Empleando cálculos de primeros principios, este estudio investiga las propiedades electrónicas, magnéticas y estructurales de estas superredes modificadas. La metodología de investigación se basa en la Teoría Funcional de la Densidad (DFT) y simulaciones DFT polarizadas por espín, utilizando la función meta-GGA r^{2}SCAN con correcciones de van der Waals, implementada en el paquete de simulación ab initio de Viena (VASP). Se examinan varias configuraciones de adatomos de H y vacantes de C en superredes de grafeno para evaluar su influencia en propiedades clave como la modulación del bandgap y el comportamiento magnético. Los hallazgos significativos resaltan el papel crucial de la posición de los adatomos de H en la alteración de la estructura electrónica y la inducción de magnetismo debido a las vacantes de C.

Palabras clave: DFT, superredes de grafeno, defecto en forma de flor, adatomos de hidrógeno, vacantes de carbono, propiedades electrónicas, propiedades magnéticas.

Abstract

Graphene is known for its exceptional electronic and structural attributes. However, its applicability in nanoelectronics and magnetic applications is constrained by its absence of a bandgap and magnetic characteristics. Given that experimental studies can be costly and time-consuming, it is essential to explore the impact of defects on graphene's properties through *ab initio* simulations. This thesis presents a computational exploration of topologically defective graphene-based superlattices, specifically focusing on the effects of hydrogen (H) adatoms and carbon (C) vacancies in the presence of a Flower-like defect (FLD). Employing first-principles calculations, this study investigates these modified superlattices' electronic, magnetic, and structural properties. The research methodology is grounded in Density Functional Theory (DFT) and spin-polarized DFT simulations, utilizing the meta-GGA r^2SCAN functional with van der Waals corrections, as implemented in the Vienna Ab initio Simulation Package (VASP). Various configurations of H adatoms and C vacancies are examined in graphene superlattices to assess their influence on key properties such as bandgap modulation and magnetic behavior. Significant findings highlight the crucial role of H adatom positioning in altering the electronic structure and the induction of magnetism due to C vacancies.

Keywords: DFT, graphene superlattices, flower-like defect, hydrogen adatoms, carbon vacancies, electronic properties, magnetic properties.

Contents

List of Figures

List of Tables

Chapter 1

Introduction

Graphene, a two-dimensional (2D) material composed of a single layer of carbon atoms arranged in a hexagonal lattice, has attracted tremendous attention in the scientific community since its discovery in 2004[1,2]. Graphene was first theorized by physicists and chemists in the 1940s and 1950s, who speculated about the stability and electronic properties of a monolayer of carbon atoms[3]. However, this theoretical abstraction only transformed into a tangible reality at the turn of the 21st century. In 2004, Andre Geim and Konstantin Novoselov successfully isolated and characterized graphene through the micromechanical cleavage technique, one of the five most commonly used exfoliation methods[4]. They used adhesive tape to peel off thin flakes of graphite, a layered material consisting of many graphene sheets stacked together. By repeatedly cleaving the graphite flakes, they could obtain graphene layers that were only one atom thick.

This discovery ignited a revolution in material science, catapulting graphene into the scientific limelight. Its extraordinary properties, such as exceptional electrical conductivity (200,000 cm^2/Vs), mechanical strength (1 TPa Young's modulus), and thermal conductivity (3000–5000 Wm/K), captured the imagination of researchers across many disciplines[3,5]. Graphene's emergence has also initiated the investigation of other emerging 2D materials, often referred to as "2D materials' science"[5]. These materials include hexagonal boron nitride (h-BN), transition metal dichalcogenides (TMDs), black phosphorus (BP), and many others. These materials have different structures and properties from graphene and can be combined with graphene to form heterostructures with novel functionalities[5].

As graphene's potential became increasingly evident, researchers and industries recognized its game-changing capabilities. Its lightweight yet robust nature makes it an ideal candidate for many applications, from flexible electronics to ultra-strong materials for construction and aerospace[3,5]. Some of the current and emerging applications of graphene include:

- Transparent electrodes for touch screens, solar cells, and light-emitting diodes (LEDs)[5].

- Sensors for detecting gases, biomolecules, and mechanical strain[5].

- Supercapacitors and batteries for energy storage[5].

- Nanocomposites for enhancing polymers, metals, and ceramics' mechanical, electrical, and thermal properties[5].

- Membranes for water purification, gas separation, and ion transport[5].

- Biomedical devices for drug delivery, tissue engineering, and biosensing[5].

1.1   Problem Statement

Despite its remarkable properties, pristine graphene has certain limitations that restrict its use in some applications, particularly in the realm of nano-electronics. One such limitation is the absence of a band gap in graphene[6]. This band gap is essential for controlling the flow of electrons, making the creation of graphene-based transistors impractical using pristine graphene.

Similarly, pristine graphene lacks inherent magnetic properties, which hinders its integration into the field of spintronics. Spintronics exploits the intrinsic spin of electrons to create devices that store and process information more efficiently than conventional electronics.

Despite these challenges, researchers have explored various strategies to engineer solutions. For instance, functionalizing graphene with various elements can introduce band gaps or induce magnetic properties[7]. Creating heterostructures by combining graphene with other materials is another approach[8]. Additionally, the utilization of topological defects in graphene structures has been considered[9].

1.2   General and Specific Objectives

We propose to study Graphene superlattices in which we integrate the Flower-like Defect (FLD) since it has been demonstrated to be a novel way of solving the bandgap opening in graphene without compromising inherent characteristics of graphene, such as its mechanical strength.

Our objective involves strategically introducing Hydrogen (H) adatoms and Carbon (C) vacancies into these superlattices. These modifications are selected based on their potential to achieve our key goals: manipulating the bandgap and introducing magnetic properties into these innovative materials.

We will employ *Ab initio* Density-Functional Theory (DFT) calculations on these structures to accomplish these objectives. This approach is expected to comprehensively understand their properties, including atomic, electronic, and potential magnetic characteristics.

1.3   Overview

This overview takes a brief look at the chapters that compose this thesis. Chapter 2 delves into the theoretical principles for comprehending DFT and its computational implementation, alongside exploring the Scanning Tunneling Microscope (STM) technique. In Chapter 3, comprehensive steps undertaken in our simulation process are

presented. Chapter 4 centers on the results derived from the simulations above. Concluding this work, Chapter 5 encapsulates an overview and conclusions, and a forward-looking perspective on potential future directions related to this project.

Chapter 2

Theoretical Background

This chapter provides comprehensive discussions not only into resolving the challenges of solving the Schrödinger equation for condensed matter systems but also into embracing the limitations involved. Within these pages, numerous concepts and ideas will be introduced, serving to progressively weave a comprehensive understanding of DFT. It is highly recommended curious readers explore the references [10–15] for an immersive exploration of this topic.

2.1 Many-body Schrödinger Equation

2.1.1 Time-Independent Schrödinger Equation

In the realm of quantum mechanics, the wavefunction $\Psi(\mathbf{r})$ emerges as one of the most crucial functions for comprehending the behavior of quantum systems [11]. To elucidate, it provides insights into the probability of locating a particle (such as an electron) within a specific position, thereby enabling predictions concerning diverse properties of macroscopic materials. The process of determining this function requires solving the Schrödinger equation, and in the context of condensed-matter systems, the most commonly employed form of this equation is its time-independent version*:

$$\hat{H}\Psi(\mathbf{r}) = E\Psi(\mathbf{r}). \tag{2.1}$$

Here, $\hat{H}$ represents the Hamiltonian operator, and $\Psi(\mathbf{r})$ constitutes a set of solutions (eigenstates) of the Hamiltonian, each associated with eigenvalues E_n.

The Hamiltonian can be represented as $\hat{H} = \hat{T} + \hat{V}$, where $\hat{T}$ is the kinetic energy operator and $\hat{V}$ is the potential energy operator. Moreover, the kinetic energy operator can be generally formulated as:

$$\hat{T} = \frac{\hat{\mathbf{p}}^2}{2m_e}. \tag{2.2}$$

---

*This version does not incorporate relativistic effects, magnetic fields, or quantum electrodynamics effects.

In this equation, m_e signifies the mass of an electron, and $\hat{\mathbf{p}}$ represents the quantum-mechanical momentum operator[†].

2.1.2   General Hamiltonian for a Condensed-Matter System

The systems of interest to us involve multiple electrons interacting with multiple nuclei. Therefore, the Hamiltonian for N electrons with coordinates $\mathbf{r}_1, \mathbf{r}_2, \ldots, \mathbf{r}_N$, and M nuclei with coordinates $\mathbf{R}_1, \mathbf{R}_2, \ldots, \mathbf{R}_M$, can be constructed as follows:

$$\hat{H} = \hat{T}_e + \hat{T}_N + \hat{V}_{e-e} + \hat{V}_{e-N} + \hat{V}_{N-N}, \tag{2.3}$$

with:

$$\hat{V}_{e-e} = \frac{1}{2} \sum_{i \neq j}^{N} \frac{1}{4\pi\epsilon_0} \frac{e^2}{|\mathbf{r}_i - \mathbf{r}_j|}. \tag{2.6}$$

$$\hat{T}_e = -\hbar \sum_{i}^{N} \frac{\nabla_i^2}{2m_e}. \tag{2.4}$$

$$\hat{V}_{e-N} = -\sum_{i,I}^{N,M} \frac{e^2}{4\pi\epsilon_0} \frac{Z_I}{|\mathbf{r}_i - \mathbf{R}_I|}. \tag{2.7}$$

$$\hat{T}_N = -\hbar \sum_{I}^{M} \frac{\nabla_I^2}{2M_I}. \tag{2.5}$$

$$\hat{V}_{N-N} = \frac{1}{2} \sum_{I \neq J}^{M} \frac{e^2}{4\pi\epsilon_0} \frac{Z_I Z_J}{|\mathbf{R}_I - \mathbf{R}_I|}, \tag{2.8}$$

where $\hat{T}_e$ represents the kinetic energy of electrons, $\hat{T}_N$ stands for the kinetic energy of the nuclei, $\hat{V}_{e-e}$ accounts for the electron-electron Coulomb repulsion interaction, $\hat{V}_{e-N}$ describes the Coulomb attraction between electrons and nuclei, and $\hat{V}_{N-N}$ denotes the nucleus-nucleus Coulomb repulsion interaction.

With this Hamiltonian in mind, the time-independent Schrödinger equation (2.1) for a condensed matter system becomes:

$$\left[-\sum_{i}^{N} \frac{\hbar^2}{2m_e} \nabla_i^2 - \sum_{I}^{M} \frac{\hbar^2}{2M_I} \nabla_I^2 + \frac{1}{2} \sum_{i \neq j}^{N} \frac{1}{4\pi\epsilon_0} \frac{e^2}{|\mathbf{r}_i - \mathbf{r}_j|} - \sum_{i,I}^{N,M} \frac{e^2}{4\pi\epsilon_0} \frac{Z_I}{|\mathbf{r}_i - \mathbf{R}_I|} + \frac{1}{2} \sum_{I \neq J}^{M} \frac{e^2}{4\pi\epsilon_0} \frac{Z_I Z_J}{|\mathbf{R}_I - \mathbf{R}_I|} \right] \Psi = E\Psi, \quad (2.9)$$

where the many body wavefunction Ψ depends on the positions of the electrons and nuclei of the system

$$\Psi = \Psi(\mathbf{r}_1, \mathbf{r}_2, \cdots, \mathbf{r}_N; \mathbf{R}_1, \mathbf{R}_2, \cdots, \mathbf{R}_M) \tag{2.10}$$

Atomic Units

Before continuing the track for understanding quantum systems, it is crucial to consider using atomic units, which proves to be highly practical when working with the Schrödinger equation, as we will demonstrate in this subsection.

As a starting point, let us consider the ground state energy of a Hydrogen atom:

$$E_{Ha} = \frac{1}{4\pi\epsilon_0} \frac{e^2}{a_0}. \tag{2.11}$$

[†]The quantum-mechanical momentum operator is given by $\hat{\mathbf{p}} = -i\hbar\nabla$, where $\hbar = \frac{h}{2\pi}$ stands for the reduced Planck constant, and $\nabla = \left(\frac{\partial}{\partial x}, \frac{\partial}{\partial y}, \frac{\partial}{\partial z} \right)$ is the Nabla vector differential operator.

where ϵ_0 is the permittivity of vacuum, e is the electron charge, and a_0 stands for the Bohr radius[‡].

Then, based on Bohr's ideas[§] and the quantization of angular momentum, we know that:

$$\hbar = m_e v \, a_0 \Rightarrow v = \frac{\hbar}{m_e a_0}. \tag{2.12}$$

where v is the electron velocity.

Consequently, it becomes natural to equate the nuclear attraction[¶] to the centrifugal force[‖]. In mathematical terms:

$$\frac{1}{4\pi\epsilon_0} \frac{e_0^2}{a_0^2} = m_e \frac{v^2}{a_0}. \tag{2.13}$$

By replacing (2.12) into (2.13):

$$\frac{1}{4\pi\epsilon_0} \frac{e_0^2}{a_0} = \frac{\hbar^2}{m_e a_0^2}. \tag{2.14}$$

Notably, the left-hand side of the equation corresponds precisely to E_{Ha}, hence:

$$\frac{1}{2} E_{Ha} = \frac{1}{2} \frac{\hbar^2}{m_e a_0^2} \Rightarrow \frac{1}{2} E_{Ha} = \frac{1}{2} m_e v^2. \tag{2.15}$$

This last equation remarks that the kinetic energy is on the order of E_{Ha}, making it convenient to normalize every term in equation (2.9) by E_{Ha}, leading us to:

$$\left[-\frac{1}{2} \sum_i^N a_0^2 \nabla_i^2 - \sum_I^M \frac{1}{2(M_I/m_e)} a_0^2 \nabla_I^2 + \frac{1}{2} \sum_{i \neq j}^N \frac{a_0}{|\mathbf{r}_i - \mathbf{r}_j|} - \sum_{i,I}^{N,M} Z_I \frac{a_0}{|\mathbf{r}_i - \mathbf{R}_I|} + \frac{1}{2} \sum_{I \neq J}^M Z_I Z_J \frac{a_0}{|\mathbf{R}_I - \mathbf{R}_I|} \right] \Psi = \frac{E}{E_{Ha}} \Psi. \tag{2.16}$$

The subsequent simplification involves setting $\frac{E}{E_{Ha}} = E_{\text{tot}}$ and adopting the units $a_0 = m_e = 1$. With these simplifications, the many-body Schrödinger equation (2.9) takes the form:

$$\left[-\frac{1}{2} \sum_i^N \nabla_i^2 - \sum_I^M \frac{\nabla_I^2}{2(M_I)} + \frac{1}{2} \sum_{i \neq j}^N \frac{1}{|\mathbf{r}_i - \mathbf{r}_j|} - \sum_{i,I}^{N,M} \frac{Z_I}{|\mathbf{r}_i - \mathbf{R}_I|} + \frac{1}{2} \sum_{I \neq J}^M \frac{Z_I Z_J}{|\mathbf{R}_I - \mathbf{R}_I|} \right] \Psi = E_{tot} \Psi. \tag{2.17}$$

From this point onward, all theoretical expressions within the Theoretical Background section will be presented in atomic units. This means that energy will be quantified in Hartrees (Ha), length will be measured in terms of Bohr radius (a_0), and masses will be scaled by the electron mass (m_e). To offer a sense of scale, below is included the conversion factors for atomic units (a.u.):

$$1 \text{ Ha} = 27.2114 \text{ eV} = 4.3597 \times 10^{18} \text{ J},$$

$$1 \ a_0 = 0.529177 \text{ Å} = 0.529177 \times 10^{10} \text{ m},$$

$$1 \text{ a. u. of mass} = 9.10938291 \times 10^{31} \text{ kg}.$$

[‡]The Bohr radius denotes the average radius of the electron orbital in a hydrogen atom.

[§]Although Bohr's atomic model (1913) has several shortcomings, the expression for the H electron energies remains remarkably accurate.

[¶]The nuclear attraction should follow the form of Coulomb's Law, given by $F = \frac{1}{4\pi\epsilon_0} \frac{q_1 q_2}{r^2}$.

[‖]The centrifugal force acting on any particle circular orbit is $F = m \frac{v^2}{r}$.

The Born-Oppenheimer Approximation

This approach, also called clamped-nuclei approximation or adiabatic approximation [13], takes advantage of the substantial differences in mass between electrons and nuclei. For instance, the lightest existing nucleus in the universe (H nucleus) weighs roughly 1800 times more than an electron [16].

Adopting this approach, the kinetic energy of nuclei can be neglected in comparison to the kinetic energy of electrons** and the Coulombic interaction between nuclei becomes a constant††. This leads to the representation of equation (2.17) as:

$$\left[-\frac{1}{2} \sum_i^N \nabla_i^2 + \frac{1}{2} \sum_{i \neq j}^N \frac{1}{|\mathbf{r}_i - \mathbf{r}_j|} - \sum_{i,I}^{N,M} \frac{Z_I}{|\mathbf{r}_i - \mathbf{R}_I|} \right] \Psi = E\Psi. \tag{2.18}$$

Defining $V_n(\mathbf{r}_i) = -\sum_I^M \frac{Z_I}{|\mathbf{r}_i - \mathbf{R}_I|}$, the many-body time-independent Schrödinger equation could be written as:

$$\left[-\frac{1}{2} \sum_i^N \nabla_i^2 + \frac{1}{2} \sum_{i \neq j}^N \frac{1}{|\mathbf{r}_i - \mathbf{r}_j|} + \sum_i^N V_n(\mathbf{r}_i) \right] \Psi(\mathbf{r}) = E\Psi, \tag{2.19}$$

where $\Psi = \Psi(\mathbf{r}_1, \mathbf{r}_2, \cdots, \mathbf{r}_N)$ only depends on the electron coordinates and the nuclear $\mathbf{R}_I$ coordinates are considered as external parameters. Moreover, from (2.19), it becomes logical to define the single-electron Hamiltonian:

$$\hat{H}_0(\mathbf{r}) = -\frac{1}{2} \nabla^2 + V_n(\mathbf{r}). \tag{2.20}$$

Hence, the many-electron Hamiltonian could be defined as:

$$\hat{H}(\mathbf{r}_1, \mathbf{r}_2, ..., \mathbf{r}_N) = \sum_i^N \hat{H}_0(\mathbf{r}_i) + \sum_{i \neq j}^N \frac{1}{|\mathbf{r}_i - \mathbf{r}_j|}. \tag{2.21}$$

Accordingly to the definition (2.21), the many-body time-independent Schrödinger equation could be written as:

$$\left[\sum_i^N \hat{H}_0(\mathbf{r}_i) + \frac{1}{2} \sum_{i \neq j}^N \frac{1}{|\mathbf{r}_i - \mathbf{r}_j|} \right] \Psi(\mathbf{r}) = E\Psi(\mathbf{r}). \tag{2.22}$$

2.1.3 Informational Challenge

Despite simplifying the many-body time-independent Schrödinger equation elegantly and straightforwardly, the difficulty of solving this equation lies in the sheer amount of information contained within the wavefunction [10].

To illustrate this challenge, let us consider a simple silicon atom. A single Si atom consists of 14 electrons, and its fully specified wave function is represented as:

$$\Psi(\mathbf{r}_1, \mathbf{r}_2, \mathbf{r}_3, .., \mathbf{r}_{14}), \tag{2.23}$$

**In practice, we can think the electrons of our system moving within a field of fixed nuclei.

††The Coulombic constant can be absorbed into $E = E_{\text{tot}} - \frac{1}{2} \sum_{I \neq J}^M \frac{Z_I Z_J}{|\mathbf{R}_I - \mathbf{R}_J|}$.

where $\mathbf{r}_i = (x_i, y_i, z_i)$, becoming $\Psi(\mathbf{r}_i)$ a function of $14 \times 3 = 42$ variables.

However, computing its wave function requires discretizing the atom. For instance, we can create a $10 \times 10 \times 10$ grid in (x, y, z) space. This approach involves describing ten complex values in each direction for every electron, resulting in 10^3 combinations for a single electron in the system. Consequently, the wave function for a single Si atom becomes a function of 1×10^{42} independent variables.

To provide an idea of the magnitude of this number, according to IDC & Statista, global data storage in 2021 amounted to approximately 5.92×10^{23} bits[††], which is not enough storage for saving the information required to describe the Si wavefunction. This comparison highlights the extreme inefficiency of the mentioned methodology and exhibits the formidable challenge that scientists have faced in creating a reliable and optimal process to compute materials.

2.2 Hartree-Fock Theory

To derive the Hartree-Fock (HF) equations, we must select an appropriate trial wavefunction and use the variational principle to minimize the energy [17]. We will begin with the simplest possible ansatz for the many-body wavefunction, a product of single-electron states as denoted in (2.24). This is referred to as the Hartree approximation. Subsequently, we will integrate the Pauli exclusion principle for electrons into our framework, eventually culminating in the complete set of HF equations [15].

2.2.1 Single-electron states

This approximation allows us to express the wavefunction of the system as the product of single-particle states:

$$\Psi(\mathbf{r}_1, \mathbf{r}_2, ..., \mathbf{r}_N) = \phi_1(\mathbf{r}_1)\phi_2(\mathbf{r}_2)...\phi_N(\mathbf{r}_N). \tag{2.24}$$

The total energy in a given state, E, can be obtained as:

$$E = \int d\mathbf{r}_1...d\mathbf{r}_2 \Psi^* \hat{H} \, \Psi. \tag{2.25}$$

Sometimes it is convenient to employ the *Dirac notation*. In this notation, equation (2.25) can be written as:

$$E = \left\langle \Psi \left| \hat{H} \right| \Psi \right\rangle. \tag{2.26}$$

For a two-electron system described by the many-electron Hamiltonian (2.21) and the product of single-particle states (2.24) in (2.26), the total energy for a given state is given by:

$$E_H[\phi_i^*, \phi_i] = \frac{1}{2} \left\langle \phi_1(\mathbf{r}_1)\phi_2(\mathbf{r}_2) \left| \hat{H}_0(\mathbf{r}_1) + \hat{H}_0(\mathbf{r}_2) + \frac{1}{\Delta r_{12}} \right| \phi_1(\mathbf{r}_1)\phi_2(\mathbf{r}_2) \right\rangle, \tag{2.27}$$

where $\Delta r_{12} = |\mathbf{r}_1 - \mathbf{r}_2|$, is the electron-electron distance.

[††]Remember that a bit is the smallest unit of data that a computer can process and store.

How can we minimize the energy of this system? In other words, what are ϕ_1 and ϕ_2 that minimize E_H? We can apply the *variational principle* using the Lagrange multipliers method. Since the energy E_H is a functional[‡‡] of the wavefunctions ϕ_i, we need to solve:

$$\frac{\delta}{\delta\phi_i^*}\left(E_H[\phi_i^*, \phi_i] - \sum_{i,j}^{N} \lambda_{ij}\left[\langle\phi_i|\phi_j\rangle - \delta_{ij}\right]\right) \tag{2.28}$$

Considering the orthonormality properties of the wavefunctions $\langle\phi_i|\phi_j\rangle = \delta_{ij}$, this simplifies to:

$$\frac{\delta}{\delta\phi_i^*}\left(E_H[\phi_i^*, \phi_i] - \sum_{i}^{N} \varepsilon_i\left[\langle\phi_i|\phi_j\rangle - 1\right]\right) \tag{2.29}$$

where each ε_i acts as a Lagrange multiplier.

Using (2.29) for a two-electron system (2.27) to minimize the energy E_H with respect to variations of the functions ϕ_1 and ϕ_2, we can derive two equations for a two-electron system:

$$\left[-\frac{1}{2}\nabla^2 + V_n(\mathbf{r}) + V_H(\mathbf{r})\right]\phi_1(\mathbf{r}) = \varepsilon_1\phi_1(\mathbf{r}). \tag{2.30}$$

$$\left[-\frac{1}{2}\nabla^2 + V_n(\mathbf{r}) + V_H(\mathbf{r})\right]\phi_2(\mathbf{r}) = \varepsilon_2\phi_2(\mathbf{r}), \tag{2.31}$$

In general, for a system of N electrons, we get:

$$\left[-\frac{1}{2}\nabla^2 + V_n(\mathbf{r}) + V_H(\mathbf{r})\right]\phi_i(\mathbf{r}) = \varepsilon_i\phi_i(\mathbf{r}), \tag{2.32}$$

where $V_n(\mathbf{r})$ is the Coulomb potential representing the electrostatic interaction between electrons and nuclei, and $V_H(\mathbf{r})$ is the Hartree potential given by:

$$V_H(\mathbf{r}) = \sum_{j} \int \frac{|\phi_i(\mathbf{r})|^2}{|\mathbf{r} - \mathbf{r}_j'|}, \tag{2.33}$$

Note that even though we use single-electron states, we get a potential experienced by the electrons[§§], which is called the Hartree potential. This new term could also be obtained throughout the mean-field approximation, a classical electrostatics approach.

2.2.2 The Exclusion Principle

Up to this point, we have ignored one of the most fundamental principles of quantum mechanics: the Pauli exclusion principle. This principle dictates that no two fermions, such as electrons, can occupy the same quantum

---

[‡‡]A functional is a function that takes another function as an argument. To distinguish a functional from a regular function, I will use square brackets for the argument, as in F[f(x)].

[§§]Essentially, we should remember that the distribution of an electronic charge will generate an electronic potential that could be added to the Hamiltonian.

state simultaneously. To incorporate this principle, it is necessary to seek a wavefunction solution using *Slater determinants*:

$$\Psi(\mathbf{r}_1, \mathbf{r}_2, ..., \mathbf{r}_N) = \frac{1}{\sqrt{N!}} \begin{vmatrix} \phi_1(\mathbf{r}_1) & \phi_1(\mathbf{r}_2) & ... & \phi_1(\mathbf{r}_N) \\ \phi_2(\mathbf{r}_1) & \phi_2(\mathbf{r}_2) & ... & \phi_2(\mathbf{r}_N) \\ \vdots & \vdots & & \vdots \\ \phi_N(\mathbf{r}_1) & \phi_N(\mathbf{r}_2) & ... & \phi_N(\mathbf{r}_N) \end{vmatrix}. \tag{2.34}$$

As a consequence, the wavefunction describing a system of electrons must be antisymmetric with respect to the exchange of any two electron coordinates. For example, if we exchange electrons $\mathbf{r}_i$ with electron $\mathbf{r}_j$, we get $\Psi(\mathbf{r}_1, \mathbf{r}_2, ..., \mathbf{r}_i, ..., \mathbf{r}_j, ...\mathbf{r}_N) = -\Psi(\mathbf{r}_1, \mathbf{r}_2, ..., \mathbf{r}_j, ...\mathbf{r}_i, ..., \mathbf{r}_N)$; this is a direct consequence of exchanging column i and j in the determinant of equation 2.34.

As before, let us consider the case of two electrons:

$$\Psi_{HF}(\mathbf{r}_1, \mathbf{r}_2) = \frac{1}{2} \left[\phi_1(\mathbf{r}_1)\phi_2(\mathbf{r}_2) - \phi_1(\mathbf{r}_2)\phi_2(\mathbf{r}_1) \right]. \tag{2.35}$$

With:

$$E_{HF} = \left\langle \Psi_{HF} \left| \hat{H} \right| \Psi_{HF} \right\rangle. \tag{2.36}$$

Applying the variational principle to (2.36) in the same manner as before, but with the new ansatz wavefunction (2.35), we can derive:

$$\left[-\frac{1}{2}\nabla^2 + V_n(\mathbf{r}) + V_H(\mathbf{r}) \right] \phi_1(\mathbf{r}) + \int V_x(\mathbf{r}, \mathbf{r}')\phi_1(\mathbf{r}')d\mathbf{r}' = \varepsilon_1 \phi_1(\mathbf{r}). \tag{2.37}$$

$$\left[-\frac{1}{2}\nabla^2 + V_n(\mathbf{r}) + V_H(\mathbf{r}) \right] \phi_2(\mathbf{r}) + \int V_x(\mathbf{r}, \mathbf{r}')\phi_2(\mathbf{r}')d\mathbf{r}' = \varepsilon_2 \phi_2(\mathbf{r}), \tag{2.38}$$

where $V_n(\mathbf{r})$ is the Coulomb potential, $V_H(\mathbf{r})$ is the Hartree potential, and $V_x(\mathbf{r})$ is the exchange potential.

In a more general setting, **for a system of N electrons**, the Hartree-Fock equations can be written as:

$$\left[-\frac{1}{2}\nabla^2 + V_n(\mathbf{r}) + V_H(\mathbf{r}) \right] \phi_i(\mathbf{r}) + \int V_x(\mathbf{r}, \mathbf{r}')\phi_i(\mathbf{r}')d\mathbf{r}' = \varepsilon_i \phi_i(\mathbf{r}), \tag{2.39}$$

where:

$$V_H(\mathbf{r}) = \sum_j \int \frac{|\phi_i(\mathbf{r})|^2}{\left| \mathbf{r} - \mathbf{r}'_j \right|}, \tag{2.40}$$

and:

$$V_x(\mathbf{r}, \mathbf{r}') = -\sum_j \frac{\phi_j^*(\mathbf{r}')\phi_j(\mathbf{r})}{|\mathbf{r} - \mathbf{r}'|}. \tag{2.41}$$

This new non-local potential called the "exchange potential" is a direct consequence of adding the Pauli exclusion principle. This shift signifies a transition from "classical" electrons in the mean field approximation to quantum electrons. $V_x(\mathbf{r}, \mathbf{r}')$ is non-local in the sense that we have to integrate over an additional variable $\mathbf{r}'$, which gives an extra degree of difficulty to Hartree-Fock equations.

2.3   Density Functional Theory

Density Functional Theory (DFT) is grounded in a variational principle, utilizing electron density as the primary physical parameter for system depiction[15]. DFT builds upon the proposition of Hohenberg and Kohn in 1964, asserting that the ground state energy of a system can be expressed as a functional dependent only on the electronic density. This innovation effectively circumvents the informational challenge by "substituting" the wavefunction—a function of 3N variables—with the electronic density $n(\mathbf{r})$, a function of only three variables.

This section will describe the two fundamental mathematical theorems for DFT stated by Kohn and Hohenberg in 1964[18], followed by the derivation of the famous Kohn-Sham equations.

2.3.1   First Hohenberg-Kohn Theorem

In the ground state, a system's total energy is a unique function of the electron density.

Proof: Let us consider the total energy for a system:

$$E = \left\langle \Psi \left| \hat{H} \right| \Psi \right\rangle = \left\langle \Psi \left| \hat{T} + \hat{W} \right| \Psi \right\rangle + \int V_n(\mathbf{r}) n(\mathbf{r}) d\mathbf{r}. \tag{2.42}$$

where $\hat{T}$ and $\hat{W}$ represents the kinetic and Coulombic potential energies respectively. The symbol for the Coulombic potential energy was changed for the convenience of the proof. The V_n term represents the external potential produced by the nuclei.

To illustrate the uniqueness of the total energy with respect to the electron density, let us consider two quantum systems, A and A'. What we want to demonstrate is whether it is possible to have both systems with the same wavefunctions (Ψ), kinetic energies ($\hat{T}$), Coulombic potential energies ($\hat{W}$), and densities ($n(\mathbf{r})$), but different external potentials (V_n).

$$
\begin{array}{cc}
\mathbf{A} & \mathbf{A'} \\
\Psi & = \Psi' \\
\hat{T} & = \hat{T}' \\
\hat{W} & = \hat{W}' \\
n & = n' \\
V_n & \neq V_n'
\end{array}
$$

The total ground state energy for system A is given by equation (2.42); similarly, for system A':

$$E' = \left\langle \Psi' \left| \hat{H}' \right| \Psi' \right\rangle = \left\langle \Psi \left| \hat{T} + \hat{W} \right| \Psi \right\rangle + \int V_n'(\mathbf{r}) n(\mathbf{r}) d\mathbf{r}. \tag{2.43}$$

Note that $\hat{T}$, $\hat{W}$, and $n(\mathbf{r})$ are the same for both systems. Since Ψ is not the ground state of V_n', then:

$$\left\langle \Psi \left| \hat{H}' \right| \Psi \right\rangle > E',$$

$$\left\langle \Psi \left| \hat{T} + \hat{W} \right| \Psi \right\rangle + \int V_n'(\mathbf{r}) n(\mathbf{r}) d\mathbf{r} > E'. \tag{2.44}$$

By summing (2.42) + (2.44), we can get:

$$E - E' > \int \left[V_n(\mathbf{r}) - V_n'(\mathbf{r}) \right] n(\mathbf{r}) d\mathbf{r}. \tag{2.45}$$

Now, similarly as before, since Ψ' is not the ground state of V_n, then:

$$\left\langle \Psi' \left| \hat{T} + \hat{W} \right| \Psi' \right\rangle + \int V_n(\mathbf{r}) n(\mathbf{r}) d\mathbf{r} > E. \tag{2.46}$$

By summing (2.43) + (2.46) , we can get:

$$E - E' > \int \left[V_n'(\mathbf{r}) - V_n(\mathbf{r}) \right] n(\mathbf{r}) d\mathbf{r}. \tag{2.47}$$

Finally, by doing (2.45) + (2.48):

$$0 > 0 \tag{2.48}$$

Reductio ad absurdum! This contradiction proves that two different external potentials cannot lead to the same ground-state density. This point was crucial for this theorem; now to complete it, let us analyze two other premises that DFT has [11]:

- The total energy is a functional of the many-body wavefunction - this signifies that the system's energy depends on its wavefunction, which is used to derive electron density and energy.

- The external potential uniquely determines the wavefunction - it has been established that the electron density in the ground state definitively dictates the external potential.

Consequently, we reach a pivotal conclusion: the total ground state energy must be a unique functional of the density, a function of three variables: $E = F[n(\mathbf{r})]$.

2.3.2   Second Hohenberg-Kohn Theorem

The electron density that minimizes $E = F[n]$, is the actual electron density of the system.

Imagine we have two different densities $n(\mathbf{r}) \neq n'(\mathbf{r})$, where Ψ corresponds to the ground state of the system. Then, the ground state energy for the system should satisfy:

$$E[n(\mathbf{r})] = \left\langle \Psi \left| \hat{H} \right| \Psi \right\rangle < \left\langle \Psi' \left| \hat{H} \right| \Psi' \right\rangle = E[n'(\mathbf{r})] \tag{2.49}$$

Consequently,

$$E[n(\mathbf{r})] < E[n'(\mathbf{r})] \tag{2.50}$$

Hence, we can ensure that true electron density minimizes the functional to the lowest possible energy. Furthermore, we can find the real electron density $n(\mathbf{r})$ of the system by applying the variational principle:

$$\frac{\delta F[n]}{\delta n} = 0 \tag{2.51}$$

where

$$F[n] = \int V_n(\mathbf{r}) n(\mathbf{r}) d\mathbf{r} + \left\langle \Psi[n] \left| \hat{T} \right| \Psi[n] \right\rangle + \left\langle \Psi[n] \left| \hat{W} \right| \Psi[n] \right\rangle \tag{2.52}$$

2.3.3 Kohn-Sham Equations

Although the Hohenberg-Kohn theorems provide the foundational insights for DFT, they need to address the functional construction directly. Additionally, the representation of Equation (2.52) presents a significant challenge due to the implicit dependence on density within the terms $\hat{T}$ and $\hat{W}$[19]. Kohn and Sham introduced innovative concepts to solve this limitation in 1965[20].

The clever idea proposed by Kohn and Sham in 1965[20] was to split the implicit terms into kinetic and Coulombic energies of non-interacting electrons plus an extra term that accounts for the difference. This leads to a functional with the form:

$$F[n] = \int V_n(\mathbf{r})n(\mathbf{r})d\mathbf{r} - \int \sum_i \phi_i^*(\mathbf{r})\frac{\nabla^2}{2}\phi_i(\mathbf{r})d\mathbf{r} + \frac{1}{2}\int\int \frac{n(\mathbf{r})n'(\mathbf{r})}{|\mathbf{r}' - \mathbf{r}|}d\mathbf{r}d\mathbf{r}' + E_{xc}[n], \qquad (2.53)$$

where the first term corresponds to the potential energy emanating from external nuclei, the second term signifies the kinetic energy of independent electrons, the third term represents the Hartree energy, and the fourth, "unknown" term is known as the *exchange and correlation energy*. The exchange energy accounts for the antisymmetry of the wavefunction due to the Pauli exclusion principle, while the correlation energy encompasses the effects of electron-electron interactions beyond the mean-field approximation.

By utilizing expression (2.53), we can apply the variational principle (2.51) to achieve the famous Kohn-Sham equations:

$$\left[-\frac{\nabla^2}{2} + V_n(\mathbf{r}) + V_H(\mathbf{r}) + V_{xc}(\mathbf{r})\right]\phi_i(\mathbf{r}) = \varepsilon_i\phi_i(\mathbf{r}) \qquad (2.54)$$

where V_n is the external nuclear potential, $V_H(\mathbf{r}) = \int \frac{n(\mathbf{r}')}{|\mathbf{r}'-\mathbf{r}|}d\mathbf{r}'$ is the Hartree potential, and $V_{xc}(\mathbf{r}) = \frac{\delta E_{xc}[n]}{\delta n}$ is the exchange and correlation potential.

Notice that KS equations split the terms into known terms and an extra unknown term, which can either lead to DFT's success or failure. All quantum many-body effects are inclusively accounted for with a precise E_{xc} term. Therefore, the key challenge lies in devising accurate approximations for the exchange and correlation functional[11].

2.3.4 DFT Functionals

DFT functionals have evolved through various generations, often visualized as rungs on Jacob's ladder[21]. Each rung represents a level of approximation and complexity, with higher rungs providing more accurate results. The five generations of DFT functionals are depicted in Table 2.1. The first rung is the Local Spin Density Approximation (LSDA), which depends solely on the local electron density. The second rung, Generalized Gradient Approximation (GGA), includes the gradient of the electron density for improved accuracy. The third rung, Meta-GGA, incorporates higher-order derivatives of the electron density. Until this rung, all the "ingredients" only required the information at local point r or infinitesimally around r, i.e., all the first three rungs are local. The fourth rung, Hybrid Functionals, mixes exact exchange from Hartree-Fock theory with GGA or meta-GGA[22]. The fifth rung, Double-Hybrids and Beyond, combines Hartree-Fock exchange, GGA, and perturbation theory for even better accuracy. Each successive rung adds complexity and computational cost but enhances the accuracy of the results.

Table 2.1: Generations of DFT Functionals on Jacob's Ladder.

Rung	Functional Type	Ingredients
Chemical accuracy		
5	Double-Hybrid Functionals	$n, \nabla n, \nabla^2 n, \tau, \psi_{occ}, \psi_{unocc}$
4	Hybrid Functionals	$n, \nabla n, \nabla^2 n, \tau, \psi_{occ}$
3	Meta-GGA	$n, \nabla n, \nabla^2 n, \tau$
2	Generalized Gradient Approximation (GGA)	$n, \nabla n$
1	Local Density Approximation (LDA)	n

The r^{2}SCAN Functional

The r^{2}SCAN functional, a meta-GGA functional type, developed by Furness *et al.*[23] presents a significant advancement in the field of computational chemistry and materials science. It is exposed as an evolution of the rSCAN[24] and SCAN[25] methodologies, designed to strike an optimal balance between computational efficiency and the accuracy of material property predictions.

The r^{2}SCAN functional aims to maintain the high accuracy levels of the SCAN functional while addressing its numerical performance issues, making it a valuable tool for large-scale chemical and materials computational studies. This development showcases the potential for improved efficiency in computational methods without sacrificing the quality of results, emphasizing its significance for future research in materials design and analysis. For instance, a study by Kingsbury *et al.*[26] evaluates the performance of the r^{2}SCAN and SCAN meta-GGA density functionals across approximately 6000 solid materials. This comparison, conducted through an automated high-throughput computational workflow, demonstrates that r^{2}SCAN achieves comparable accuracy to SCAN in predicting band gaps and degrees of electron localization but predicts systematically larger lattice constants. It achieves superior accuracy in formation energies while also offering significantly improved numerical stability (more reliable convergence) and computational efficiency. These findings underscore r^{2}SCAN's potential as a general-purpose, numerically robust meta-GGA functional for extensive material property predictions.

The r^{2}SCAN meta-GGA functional can be effectively combined with the Revised non-local van der Waals density functional (rVV10)[27] to extend its applicability in computational studies.

A benchmark study[28] has demonstrated that the combination of r^{2}SCAN and rVV10 (r^{2}SCAN+rVV10) is suitable for general-purpose solid-state materials discovery. This combination improves the treatment of dispersion interactions without compromising the accuracy of formation enthalpy predictions and even modestly enhances cell volume predictions. However, it is important to note that both r^{2}SCAN and r^{2}SCAN+rVV10 tend to underestimate the fundamental band gaps of insulators, with r^{2}SCAN occasionally overestimating the band gaps of narrow-gap insulators. Despite this, r^{2}SCAN+rVV10 does not introduce significant errors and is particularly recommended for layered materials.

The integration of r^{2}SCAN with rVV10 enables the precise treatment of dispersion interactions, which are particularly important in our systems where van der Waals forces, such as those arising from the 2pz states of

graphene, can play a significant role, especially in the context of interactions with hydrogen adatoms.

2.3.5   Spin in Density Functional Theory

As described in Giustino's book[11], the adaptation of the Hohenberg–Kohn theorem to spin-dependent DFT (spin-DFT) is characterized by the following key aspect: the total energy becomes now a functional dependent on both the electron density and the spin density. So, it can be represented as:

$$E = G[n(\mathbf{r}), s(\mathbf{r})] \tag{2.55}$$

This approach is an extension of the principles found in non-magnetic DFT. In the context of spin-polarized DFT, the electron density is conceptualized as an aggregation of the charge and spin densities of independent two-component spinors. By simplifying these ideas, we can encapsulate them in a *density matrix*, expressed as:

$$n_{\alpha\beta}(\mathbf{r}) = \sum \phi_i^*(\mathbf{r}; \alpha)\phi_i(\mathbf{r}; \beta), \tag{2.56}$$

Here, α and β are integers, usually 1 or 2, denoting the spinor components.

Furthermore, the ground-state energy functional is represented by:

$$E = G[n_{\alpha\beta}(\mathbf{r})] \tag{2.57}$$

In the same manner as conventional DFT, spin-DFT employs the Kohn-Sham formalism. This formalism states that the ground-state density matrix, $n_{\alpha\beta}^0$, minimizes the functional G, as shown in:

$$\left. \frac{\delta G[n_{\alpha\beta}(\mathbf{r})]}{\delta n_{\alpha\beta}(\mathbf{r})} \right|_{n_{\alpha\beta}^0} = 0 \tag{2.58}$$

By ensuring the orthonormality of the spinors, we derive a relationship similar to the Kohn-Sham equations for spin-DFT:

$$\left[-\frac{\nabla^2}{2} + V_n(\mathbf{r}) + V_H(\mathbf{r}) + V_{xc}(\mathbf{r}) + \mu_\beta \sigma \cdot \mathbf{B}_{xc}(\mathbf{r}) \right] \phi_i(\mathbf{r}) = \varepsilon_i \phi_i(\mathbf{r}) \tag{2.59}$$

This equation is crucial in the Kohn-Sham framework for spin-DFT, highlighting the role of the exchange and correlation magnetic field $\mathbf{B}_{xc}(r)$, which emerges due to the collective magnetic interactions among electrons. This additional field is instrumental in aligning electron spins, that might induce magnetic order in the system.

2.4   DFT Computational Implementation

This section describes the foundational concepts behind the practical implementation of DFT calculations, focusing on the Vienna *Ab initio* Simulation Package (VASP)[29,30]. By delving into these concepts, we can understand how DFT is practically realized within the framework of computational simulations.

2.4.1 Basis set: Plane Waves

Vasp is a plane-wave code that efficiently perform simulations in periodic systems but it can be applied to molecules or clusters. In this context, solutions to the Schrödinger equation in a periodic potential can be expressed as a product of a plane wave and a function that exhibits the periodicity of a Bravais lattice*** – a concept introduced by Felix Bloch in 1928[31]. These functions are known as Bloch functions and are characterized by the following form:

$$\phi_{n\mathbf{k}}(\mathbf{r}) = e^{i\mathbf{k}\cdot\mathbf{r}}u_{n\mathbf{k}}(\mathbf{r}) \tag{2.60}$$

where n is the band index, $\mathbf{k}$ represents a vector in the Brillouin Zone (BZ), and $u_{n\mathbf{k}}(\mathbf{r})$ is a periodic function on the Bravais lattice. This periodic function can also be expanded in terms of plane waves, labeled according to the reciprocal lattice vectors:

$$u_{n\mathbf{k}}(\mathbf{r}) = \sum_{\mathbf{G}} C_{n\mathbf{k}}^{G}e^{i\mathbf{G}\cdot\mathbf{r}} \tag{2.61}$$

where $\mathbf{G}$ is a reciprocal vector defined by $\mathbf{G}=m_1\mathbf{b}_1+m_2\mathbf{b}_2+m_3\mathbf{b}_3$ with integres values for m_i.

Although several other basis sets are available, such as Gaussian basis sets, real-space representations, and linear combination of atomic orbitals (LCAO), the plane-wave basis set can highlight some advantages. For instance, it allows for systematic resolution improvement by adding more plane waves, enables easy evaluation of gradients and laplacians, and maintains basis set independence from atomic positions.

Kinetic Cutoff and k-points

The challenge in constructing a plane wave basis set lies in selecting an appropriate maximum cutoff kinetic energy for the electrons and discretizing the k-space. These parameters play a fundamental role in balancing precision and computational efficiency.

Mathematically, the maximum cutoff kinetic energy (E_{cut}) is related to the highest allowed $\mathbf{G}$-vector, denoted as $\mathbf{G}_{max}$, by the equation:

$$E_{cut} = \frac{1}{2}\mathbf{G}_{max}^2 = \left\langle e^{i\mathbf{G}_{max}\cdot\mathbf{r}} \left| \frac{1}{2}\nabla^2 \right| e^{i\mathbf{G}_{max}\cdot\mathbf{r}} \right\rangle \tag{2.62}$$

A higher cutoff energy includes a larger number of $\mathbf{G}$-vectors, leading to improved precision in representing high-frequency wavefunctions and electron density features. However, this also increases the computational effort required for calculations. Therefore, selecting an appropriate E_{cut} involves a delicate trade-off, which is precisely why a convergence criterion is required.

For the determination of the appropriate k-point mesh, several methods are available, among which the Monkhorst-Pack method (MP) stands out[32,33]. The MP method generates sets of k-points within the Brillouin Zone (BZ), offering an effective approach for integrating periodic functions involving the wave vector. Nevertheless, achieving an optimal k-point mesh also entails adhering to a convergence criterion; this involves iteratively calculating the total energy per atom and gradually adding k-points until the convergence criterion is met.

***Bravias lattice can be thought as an infinite array of points where the environment of any given point is equivalent to the environment of any other given point.

2.4.2   Pseudopotentials

The idea of the pseudopotential is to replace the full nuclear potential with a practical and accurate approximation. Given that the valence electrons are the primary contributors to bonding[†††], a pseudopotential can be formulated by considering a specific core radius; this is also called the frozen core approximation. This radius allows us to approximate the shielding effect of the core electrons on the valence electrons from the nuclear potential.

Current DFT codes offer a library of pseudopotentials that includes an entry for each element on the periodic table. Pseudopotentials requiring lower cutoff energies are more computationally efficient than those necessitating higher energies. Among the various methods available for defining pseudopotentials, the ultra-soft pseudopotentials (USPPs) are the most widely employed because they require significantly lower cutoff energies than other alternatives.

One disadvantage of using USPPs is that constructing the pseudopotential for each atom requires the specification of several empirical parameters. An approach that avoids some of the disadvantages of USPPs is the projector augmented-wave (PAW) method[34].

2.4.3   The Projector Augmented-Wave (PAW) Method

The PAW method aims to address some limitations associated with constructing pseudopotentials. In the PAW method, all-electron wave functions are constructed with the help of auxiliary functions called projectors, providing a more accurate description of both core and valence electrons.

This method, available in VASP, balances accuracy and computational efficiency, making it well-suited for studying a wide range of materials and properties. It has become a popular choice in electronic structure calculations, particularly in cases where a high level of accuracy is required, such as in complex chemical reactions or materials with challenging electronic structures[35].

2.4.4   Two-dimensional equation of state

The two-dimensional equation of state (2D EOS) proposed by R. C. Andrew *et al.*[36] provides a means to relate the energy to the change in surface area of a two-dimensional lattice. The 2D EOS is given by:

$$E(A) = E_0 + 4A_0\gamma_0 \left(\frac{1}{2}\epsilon^2 + \frac{1}{3}(5 - \gamma_0')\epsilon^3 + \frac{1}{6}\left[(1 - \gamma_0')(8 - \gamma_0') + \gamma_0\gamma_0'' + 18 \right]\epsilon^4 \right), \tag{2.63}$$

where $A_0, \gamma_0, \gamma_0', \gamma_0''$, and ϵ are the equilibrium values for the unit-cell area, layer modulus, the force per unit length derivative, the second derivative of the layer modulus at $F = 0$, and the equibiaxial Eulerian strain is given by:

$$\epsilon = \frac{1}{2}\left[1 - \frac{A_0}{A} \right] \tag{2.64}$$

This process involves calculating the energy for various lattice constants, plotting the energy against the corresponding area, and then fitting the 2D EOS to find the ground-state energy, which gives the optimal lattice constant. The EOS also provides the layer modulus, indicating the 2D material's resistance to uniform stretching. This is analogous to the bulk modulus in bulk materials, which measures resistance to compression.

[†††]There are some elements as Bismuth where we should be careful how we define the valence electrons.

2.5   Scanneling Tunneling Microscopy

2.5.1   Working Principle

Scanning Tunneling Microscopy (STM) operates by regulating the tunneling current that traverses the potential barrier between the sample surface and the probing metal tip. This technique capitalizes on the principles of quantum tunneling. A tunneling current emerges by applying a bias voltage between the tip and the surface as the gap between them is reduced to a few atomic diameters.

The STM can operate in either constant-current mode or constant-height mode[37]. The tip-to-sample distance is adjusted to maintain a consistent current while the tip scans the sample surface in the constant-current mode. This process yields a topographic image of the sample by recording and processing the tip's height variations.

In contrast, the height-constant mode involves scanning the tip over the surface while maintaining nearly constant height and voltage, monitoring the tunneling current. The fluctuations in tunneling current resulting from the tip encountering surface features are detected and graphed as a function of the scanning position. This mode provides valuable insights into the sample's local electronic properties and surface structures.

2.5.2   Tersoff-Hamann approximation

The Tersoff-Hamann approximation[38], a method integral to surface science, simplifies the calculation of electronic properties at solid surfaces. This approach is particularly relevant in scanning tunneling microscopy (STM), which helps understand the tunneling current between a metallic tip and the sample surface. The approximation makes a simplified assumption about the tip's electronic structure, thereby providing insights into the electronic behavior of surfaces.

The approximation treats the tip's electronic states as localized and represented by a single energy level. This level corresponds to the energy required for an electron to move from the tip into the vacuum and is determined by the work function of the tip material. In this context, the tunneling process is conceptualized as an electron transfer between this localized level and the surface states of the sample. The mathematical expression that captures the variation of the tunneling current with the tip-surface distance is given by:

$$I \propto \sum_k \left| \langle \Psi_k^{tip} | \Psi_n^{surf} \rangle \right|^2 \delta(E_k^{tip} - E_n^{surf} - eV). \tag{2.65}$$

In this equation, I denotes the tunneling current, Ψ_k^{tip} signifies the wave function of the tip electron with energy E_k^{tip}, and Ψ_n^{surf} represents the wave function of the surface state with energy E_n^{surf}. The term eV stands for the applied bias voltage. The overlap integral $\left| \langle \Psi_k^{tip} | \Psi_n^{surf} \rangle \right|^2$ indicates the probability of electron tunneling, and the summation extends over all possible tip electron states, denoted as k.

While the Tersoff-Hamann approximation simplifies the mathematical description of tunneling, it mainly offers a qualitative understanding of how the tunneling current changes with distance. Its simplicity, however, may only capture some intricacies of the electronic interactions, especially in cases where the tip's electronic structure is complex or when chemical interactions are significant. For example, more sophisticated models would yield more accurate results in scenarios involving strong covalent bonding or significant spin-polarization effects.

Chapter 3

Methodology

3.1 VASP Workflow

This section will explain the methodology underpinning our investigations for performing practical DFT calculations using VASP. Additionally, I will delve into the diverse outputs and results that can be obtained from these calculations.

3.1.1 Graphene Supercells Creation – POSCAR

Within VASP, the file containing a material's lattice geometry and ionic positions is named POSCAR[39]. Therefore, constructing this file is the first step for conducting DFT simulations. In the case of pristine graphene, an extensively studied material, various databases host this file detailing its structure. Pristine graphene is characterized by a honeycomb arrangement made of hexagons, and its primitive unit cell comprises two atoms connected by a bond length of 1.42 Å. The Fig. A.1 showcases the POSCAR representation of pristine graphene.

To create the FLD, graphene supercells were formed by replicating the pristine graphene's unit cell by N×N times, with N representing the original unit cell. The FLD is essentially the result of rotating a 24-carbon section to the lattice, which reconfigures covalent bonds to form pentagon and heptagon structures within the flower-like arrangement. The method used for bond recalculation is based on distance criteria, where atoms within a predefined cutoff distance specific to their element types are considered bonded. This process can be done using software tools that manipulate atoms, such as ASE or Material Studio, as shown in Figure 3.1. Moreover, within the same manipulation tool, we can introduce H adatoms or create C vacancies within the structure, saving the structure as a POSCAR file, ready for use in our DFT calculations. However, the atomic structure of the systems is computed to generate the equation of states described in section 2.4.4 that considered the relaxation of the internal coordinates and the lattice parameters.
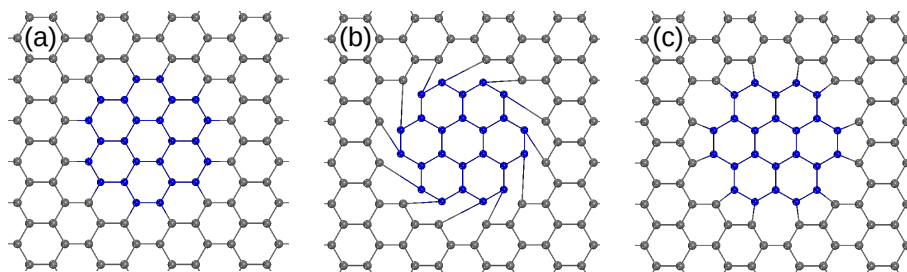
Figure 3.1: Construction of the FLD defect. (a) The initial selection of 24 C atoms (blue ones), followed by (b) an in-plane rotation of 30°, and (c) subsequent bond recalculation.

3.1.2   Selecting the Potentials – POTCAR

The POTCAR file is a repository of pseudopotentials for each atomic species incorporated in the calculation[40]. These pseudopotentials, including the projector augmented wave (PAW) potentials, can be accessed through the VASP Portal for all elements in the periodic table. For this thesis, PAW potentials for both C and H were employed. When studying a structure with different types of atoms, it's essential to concatenate the potentials within a unique POTCAR file, preserving the order specified in the POSCAR file.

3.1.3   VASP Directives – INCAR

The instructions for implementing the different routines in the VASP software should be specified in the INCAR file[41]. Among the essential simulation parameters, we have:

- **Cutoff Energy:** Through a convergence process employing a criterion of 1 meV per atom, we determined the optimal cutoff energy to be `ENCUT = 950` eV as illustrated in Figure 3.2.

- **Exchange-Correlation Energy Functional:** In our case, we utilized the r^2SCAN functional well-suited for our specific simulation needs.

- **Corrections:** In order to enhance the precision of the simulation results, various correction factors were applied. For instance, in this work, van der Waals interactions were considered.

- **Relaxation Calculation:** All structures underwent full relaxation. The optimal structure was achieved by setting `EDIFFG=0.01`, ensuring that the relaxation continues until each atom's forces are less than 0.01 eV/Å.

- **Electronic Properties Calculation:** Different tags exist for calculating a range of electronic properties of the simulated system. For instance, `LORBIT=11` enables the calculation of the projected density of states.

- **Magnetic Parameters:** A critical aspect of simulating magnetic properties is the specification of the spin polarization. For example, setting `ISPIN=2` enables spin-polarized calculations. This flag allows for the

differentiation between spin-up and spin-down electrons, thereby enabling the study of magnetic moments and spin-dependent electronic structures. More documentation about INCAR tags can be found here [41].
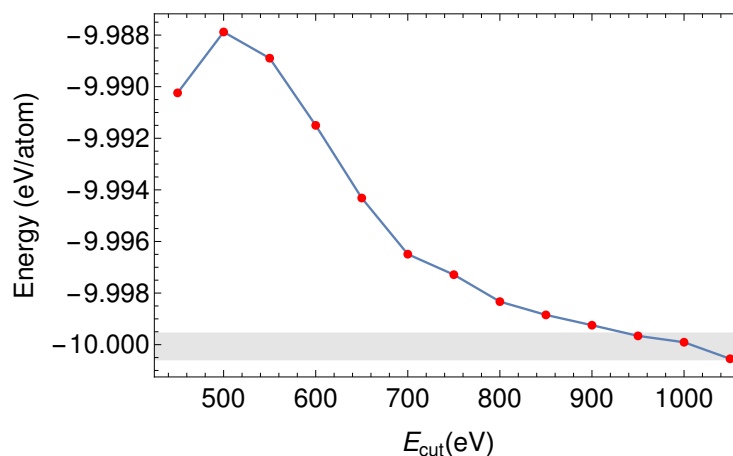

Figure 3.2: Total energy convergence as a function of the kinetic cutoff energy. The grey color indicates an energy range of 1 meV. Therefore, the cutoff energy used for graphene was 950 eV. The shape that follows the date does not have any physical meaning but only help us to find out the convergency cutoff energy.

3.1.4   Convergency process for KPOINTS

The KPOINTS file specifies the Bloch vectors (k-points) used for sampling the Brillouin zone [42]. In this context, we check the convergence of the total energy per atom to set the k-points. The results, presented in Figure 3.3, indicate that the optimal converged number of k-points is $19 \times 19 \times 1$[¶¶]. The total energy can fluctuate as the number of k-points increases, but the important feature is the convergence of the total energy with respect to the number of k-points as depicted in Figure 3.3. In this study, it is essential to account for the Dirac Point to prevent false band gaps in the density of states, considering the abrupt change in dispersion at the Dirac point.

After analyzing the inclusion of the Dirac point, we opted for a grid of $21 \times 21 \times 1$ k-points. Furthermore, since our study focuses on graphene superlattices, it is optimal not to repeat the convergence process every time we construct a new superlattice. Instead, we conserve the same k-point distance obtained from pristine graphene, which turns out to be $2\pi \times 0.022$ Å^{-1}.

3.1.5   VASP Outputs

VASP offers a variety of outputs. However, the most used ones are the CONTCAR, OUTCAR, OSZICAR, DOSCAR, PROCAR, and WAVECAR files.

[¶¶]The z-axis contains a single k-point since we are working with a 2D material.
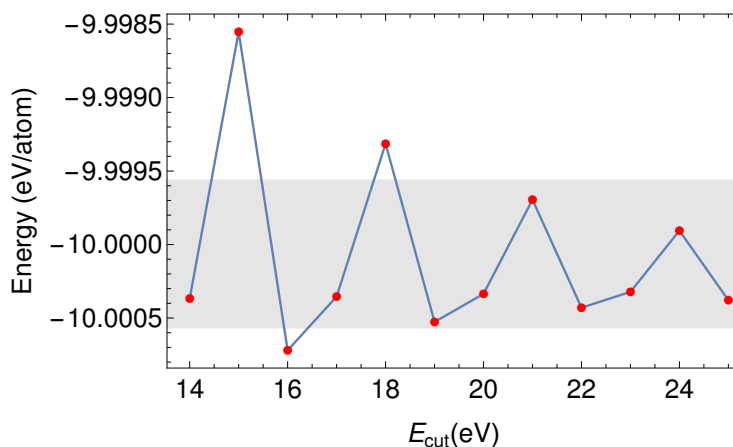
Figure 3.3: Energy convergence as a function of number of *k*-points. The grey color indicates an energy range of 1 meV. Therefore, the *k*-point mesh used for graphene was 21×21×1, since it includes the Dirac Point.

CONTCAR

In the cases where the structure relaxation is performed, the CONTCAR file contains the positions attained during the final ionic relaxation step[43]. We select various lattices close to the expected optimal lattice and allow VASP to calculate the corresponding CONTCARs for each lattice. Using these calculated CONTCARs, we apply the 2D EOS described in subsection 2.4.4 to determine the optimal lattice. For instance, the 2D EOS for pristine graphene is illustrated in Fig. 3.4.

OUTCAR

The OUTCAR file provides an elaborate output from a VASP computation, including a summary of the input parameters utilized, details concerning the electronic iterations, KS-eigenvalues, stress tensors, and more[44].

OSZICAR

This file details the results, including factors such as the convergence status of total energy, free energies, etc[45].

DOSCAR

The DOSCAR file provides a comprehensive density of states (DOS) analysis, supplying information about the distribution of energy states within the electronic structure of the system[46]. It includes data on individual atoms' total and partial DOS (PDOS) contributions.
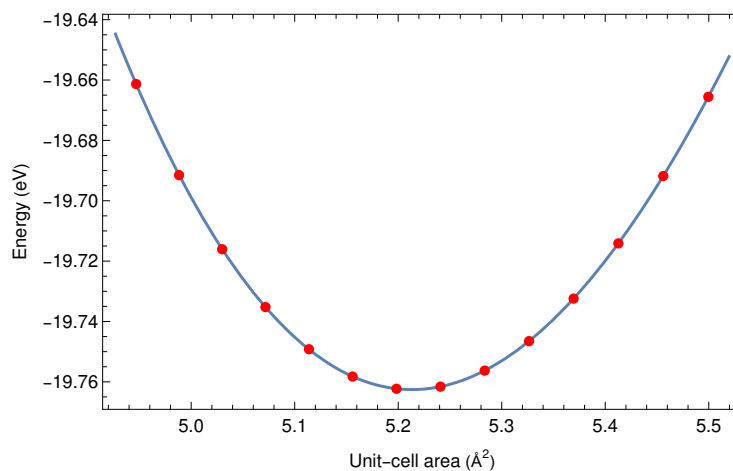
Figure 3.4: r^{2}SCAN+rVV10 computed 2D EOS fitted to the energy versus the unit-cell area. The curve illustrates the relationship between the total energy and the unit-cell area enabling the determination of the optimal lattice constant at the ground-state.

PROCAR

The PROCAR file contains the spd- and site-projected wave function character of each orbital, along with information about the number of k-points, bands, and the number of ions considered[47]. This file enables us to plot the band structure and conduct analysis.

3.2 STM Simulations

In this section, we explore the STM simulations using the bSKAN software. We explore both the inputs required for the simulation and the outputs obtained from the bSKAN simulation.

3.2.1 bSKAN Inputs

When setting up a bSKAN simulation for STM, several inputs are essential to model tunneling behavior accurately and generate meaningful results. These inputs include the tip-sample distance, bias voltage, and atomic and electronic structure information. A significant advantage of using the bSKAN code is its ability to utilize a variety of input and output files from VASP. We employ the CONTCAR file obtained from DFT calculations for the atomic structure. The OUTCAR and INCAR files from VASP are also essential. Specifically, the INCAR file requires an additional line to enable STM simulation integration. The output wavefunctions, stored in the WAVECAR file, are critical inputs for the Tersoff-Hamann approximation framework. Additionally, an INSCAN file is used to specify technical details for the STM calculation, such as the bias voltage, number of grid points, and other relevant parameters[48].

Proper configuration of these inputs ensures that the simulation accurately represents the interaction between the STM tip and the sample surface. This accurate representation is key to gaining insights into the nanoscale's surface morphology and electronic properties.

3.2.2 bSKAN Outputs

Upon completing a bSKAN simulation, it generates various outputs, each offering insights into the simulated STM process. However, in this research, the primary focus is on the OUTSCAN and CURRENT files. The OUTSCAN file compiles all the output information from the simulation, providing an overview of the simulated STM interaction. On the other hand, the CURRENT file contains the current matrix in OpenDX format. This file is essentially a grid that maps the distribution and intensity of the tunneling current across the simulated surface, offering a detailed visualization of the electronic behavior at the surface.

In this study, we have utilized Wolfram Mathematica to interpolate functions based on the simulation data and visualize the surfaces obtained. This approach allows the identification of surface features, enhancing the ability to interpret and compare with future experimental STM data. For example, the visualizations generated can be instrumental in analyzing specific features on the surface, such as defects, adsorbates, or variations in electronic density.

Chapter 4

Results & Discussion

4.1   Pristine Graphene

The initial phase of this study involved replicating the results for pristine graphene, as reported in numerous prior studies, using the methodologies described in the preceding section. Pristine graphene is characterized by a unit cell comprising two atoms. The results obtained were highly consistent with computational and experimental studies[49,50], as illustrated in Fig. 4.1. The computed band structure of pristine graphene shown in Fig. 4.1(b) was in excellent agreement with established data[49], showcasing the robustness of our simulation techniques. The Dirac cone at the Dirac point (K) is a critical feature of pristine graphene, indicative of its unique electronic properties, which were accurately reproduced in our results. Moreover, the Density of States (DOS) analysis also demonstrates the semimetallic behavior of pristine graphene. The DOS profile aligns with the expected theoretical models[49], further validating our simulation processes' accuracy.

Additionally, the STM images successfully captured the distinctive honeycomb lattice of pristine graphene, clearly showing the positions of the carbon atoms, as depicted in Fig. 4.1(a, c). An interesting aspect to highlight is that at a bias voltage of 0.9V, the STM images show enhanced quality, with significant brightness on the carbon atom sides, further elucidating the lattice structure. These simulated STM images are also in agreement with experimental images[50], confirming the precision of the simulation methods used.
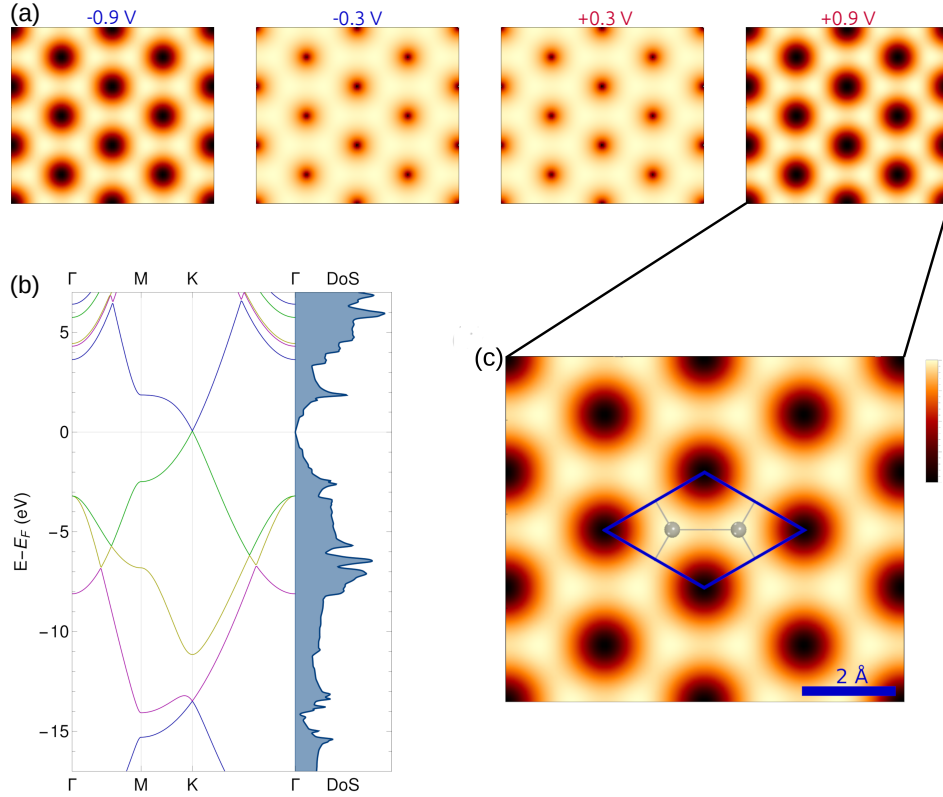
Figure 4.1: (a) Simulated STM images for pristine graphene for a bias voltage range from -0.9 V to +0.9V, highlighting the bright sites that indicate the location of the carbon atoms. (b) r^2SCAN+rvv10 computed band structure of pristine graphene along the high symmetry points, accompanied by the computed density of states (DOS). (c) STM image at a bias voltage of +0.9V (empty states), with the blue rhombus denoting the primitive cell of the structure.

4.2   Bandgap Manipulation in Graphene based Superlattices

After verifying the accuracy of our methods with pristine graphene, we shifted our focus to graphene superlattices. The motivation for exploring H adatoms in the Flower-Like Defects (FLD) came to light from the work of Garzón *et al.*[51]. This study highlighted a significant contribution of the $2pz$ orbitals from the edge carbon (C) atoms in the FLD to the electronic structure. Consequently, we expected that H adatoms positioned at the FLD borders would considerably influence the electronic structure of the superlattices.

Another intriguing subject was the Moiré-like H pattern reported by Balog *et al.*[52]. Their findings demonstrated a notable alteration in the electronic structure, prompting us to investigate these H configurations and these two

distinct regions within this pattern separately. Ultimately, we chose to analyze three specific areas to assess the impact of H adatoms on the electronic structure: the border, the inner region, and the outer region of the flower-like pattern, as illustrated in Fig. 4.2.
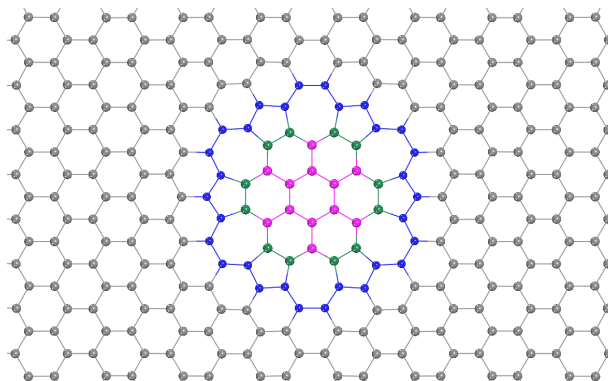
Figure 4.2: (a) Border (green), (b) inner (magenta), and (c) outer (blue) atoms of the FLD.

Within the regions illustrated in Fig. 4.2, different patterned H configurations were tested for this specific superlattice, changing the sites, directions, and numbers of the H adatoms. It is worth mentioning that after some calculations, we concluded that the inclusion of H adatoms just within the inner region of the FLD had a negligible impact on the electronic structure of the system. Thus, we have omitted such cases from our report. Nevertheless, when H adatoms are positioned at the edges and exterior of the FLD, the bandgap experiences an increase and diminishes, respectively.

4.2.1   H Adatoms on the FLD's Edge

The 6×6 Graphene Superlattices

Three different hydrogen (H) configurations were explored within the region depicted in Fig.4.2(a). The first, denoted as 6×6-FLD-12h, represents a configuration where all the H adatoms have the same orientation (Fig.4.3(a)). The second, labeled as 6×6-FLD-12hud, corresponds to a configuration in which two H adatoms are oriented upward, followed by the next two oriented downward (Fig.4.3(b)). Finally, the third configuration, called 6×6-FLD-12hudu, involves the alternation of H adatoms between upward and downward orientations (Fig.4.3(c)). It is important to note that this variation in the orientation of H adatoms has the potential to impact not only the electronic structure but also the stability of the material.

Fig.4.7(b) and Fig. 4.8(b) show the r^{2}SCAN+rVV10 computed electronic structure and band structure for system 6×6-FLD-12h (Fig. 4.3(a)), respectively. Considering the DOS displayed in Fig. 4.7 violet line, the predicted bandgap is ~1.16 eV (*cf.* Table 4.1). Analysis of the PDOS presented in Figs. A.4 and A.5 reveals that the peak at approximately ~-0.3 eV predominantly consists of $2pz$ states from carbon atoms at and near the boundary of the FLD, with an additional small contribution from the $1s$ states of H adatoms. Similarly, the peak at approximately
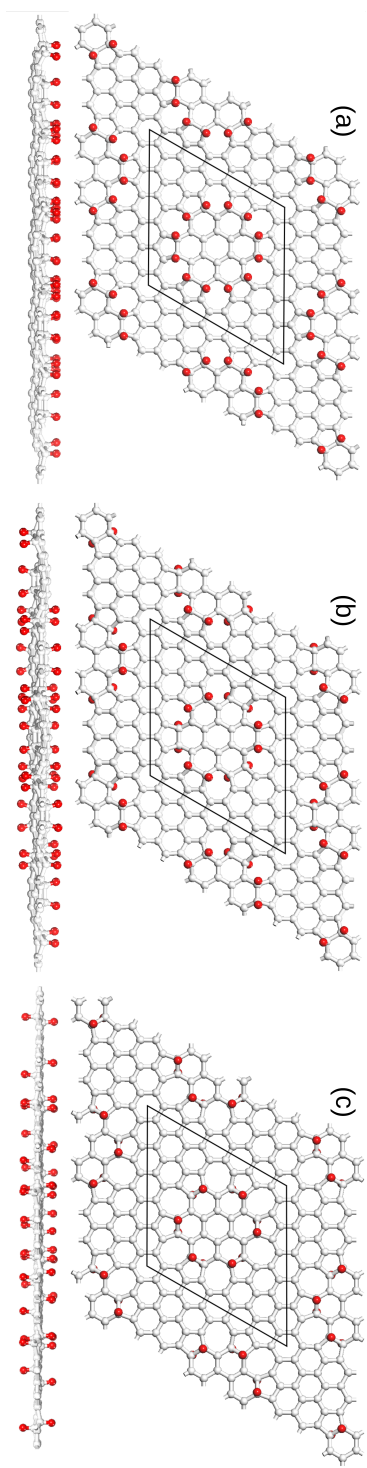
Figure 4.3: Top view and side view of: (a) Configuration 6×6-FLD-12h, where all H adatoms have the same orientation. (b) Configuration 6×6-FLD-12hud, with two H adatoms oriented upward followed by the next two oriented downward. (c) Configuration 6×6-FLD-12hudu, involving alternation of H adatoms between upward and downward orientations.

~+1.6 eV is characterized by a similar composition formed mainly of *pz* states. This observation is corroborated by simulated STM images, as shown in Fig. 4.4(b) where the bright regions are due to the protrusion of the *pz* states into the vacuum.
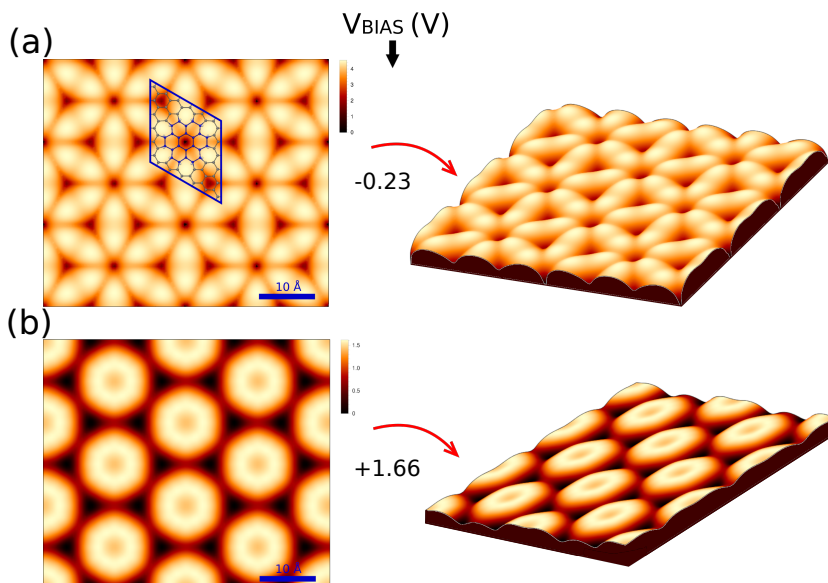
Figure 4.4: Computed scanning tunneling microscopy (STM) images for the 6×6-FLD-12h structure, highlighting the electronic states at bias voltages of (a) ~-0.23 V (occupied states) and (b) ~+1.66 V (unoccupied states). The images on the right further demonstrate STM's capability to produce three-dimensional visualizations, enabling detailed analysis of the material's topography.

Similarly, the electronic and band structures for the 6×6-FLD-12hud and 6×6-FLD-12hudu systems, as computed with the r²SCAN+rVV10 functional, are depicted in Figs. 4.7(c-d) and Figs. 4.8(c-d), respectively. The analyses focus on the distinct predicted bandgaps—approximately 1.09 eV for the 6×6-FLD-12hud (highlighted by the yellow line in Fig. 4.7) and 1.12 eV for the 6×6-FLD-12hudu (indicated by the green line), as corroborated by Table 4.1.

The PDOS analyses for both systems are illustrated in Figs. A.6 - A.9, reveal a consistent peak around ~-0.2 eV, predominantly composed of 2*pz* states from carbon atoms at and adjacent to the FLD boundary, complemented by small contributions from the 1*s* states of H adatoms. Furthermore, peaks observed at approximately ~+1.2 eV for both configurations underscore a similar compositional pattern. These findings gain further validation from simulated scanning tunneling microscopy (STM) images (Fig. 4.5 and 4.6), which offer additional insights into the localized electronic states and the material's topography.
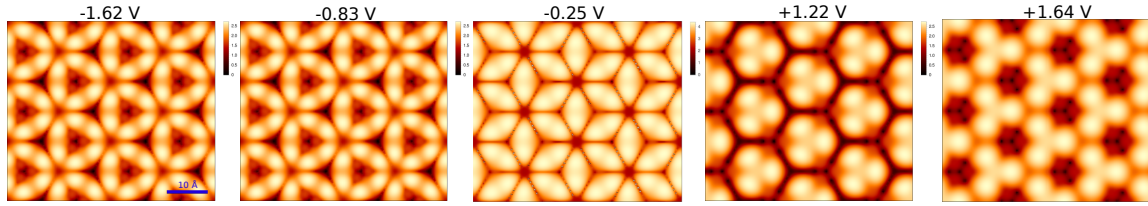
Figure 4.5: Computed scanning tunneling microscopy (STM) images for the 6×6-FLD-12hud structure at different bias voltages.
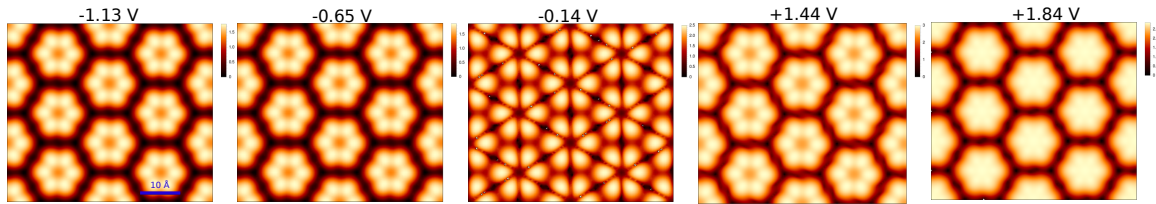
Figure 4.6: Computed scanning tunneling microscopy (STM) images for the 6×6-FLD-12hudu structure at different bias voltages.

Further analysis of all band structures depicted in Fig. 4.8 reveals that the bands around the Fermi level exhibit minimal dispersion, indicating that the corresponding electronic states are localized. This observation suggests a strong localization of charge carriers near the Fermi level in these systems.

Additionally, the EOS computations for these 2D systems enable the estimation of the layer modulus, γ_0, a parameter that quantifies the mechanical strength of these superlattices. As indicated in Table 4.1, the presence of topological defects, both with and without H adatoms, generally reduces mechanical strength compared to pristine graphene. Notably, the 6×6 FLD superlattice demonstrates superior mechanical strength compared to variants with H adatoms. This outcome can be attributed to the fact that H adatoms likely reduce the electron density around carbon-carbon (C-C) covalent bonds, thereby diminishing the overall strength of the 2D lattice.
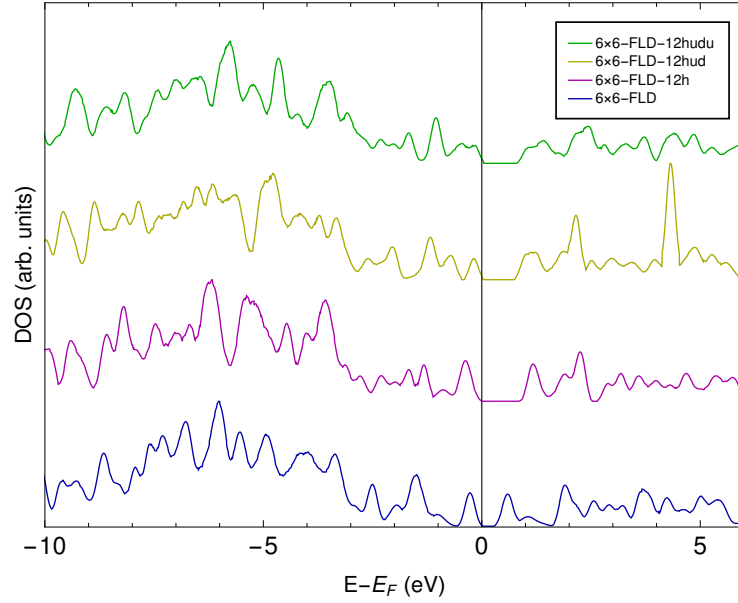
Figure 4.7: r^2SCAN+rVV10 computed DOS for the different 6×6 FLD superlattices with H adatoms configurations on the FLD's Edge. The (a) blue line represents the DOS of 6×6-FLD, (b) violet line corresponds to 6×6-FLD-12h, (c) yellow line to 6×6-FLD-12hud, and (d) green line to 6×6-FLD-12hudu.

Table 4.1: Structural and electronic r^2SCAN+rvv10 computed properties of 6×6 FLD superlattices with H adatoms on the edge. a_0 represents the optimal lattice parameter, E_g is the bandgap, N_C is the number of carbon atoms, N_H is the number of hydrogen adatoms, ΔE_c is the cohesive energy, γ_0 is the layer modulus, and Symmetry indicates the crystal symmetry.

System	a_0 (Å)	E_g (eV)	N_C	N_H	ΔE_c(eV/atom)	γ_0 (N m^{-1})	Symmetry
Pristine	2.4535	0	2	0	-7.493	216.96	$P6/mmm$ (191)
6×6-FLD	14.817	0.63	72	0	-7.386	195.72	$P6mm$ (183)
6×6-FLD-12h	14.749	1.16	72	12	-6.232	109.55	$P6mm$ (183)
6×6-FLD-12hud	14.696	1.09	72	12	-6.255	97.66	$P3m1$ (156)
6×6-FLD-12hudu	14.915	1.12	72	12	-6.241	185.10	$P6$ (168)

The 5×5 and 7×7 graphene superlattices

To further explore the viability for opening the bandgap of the H configurations illustrated in Fig. 4.3, simulations were also conducted on the 5×5 and 7×7 superlattices with identical H configurations (Fig. 4.9(a-f)). Contrary to
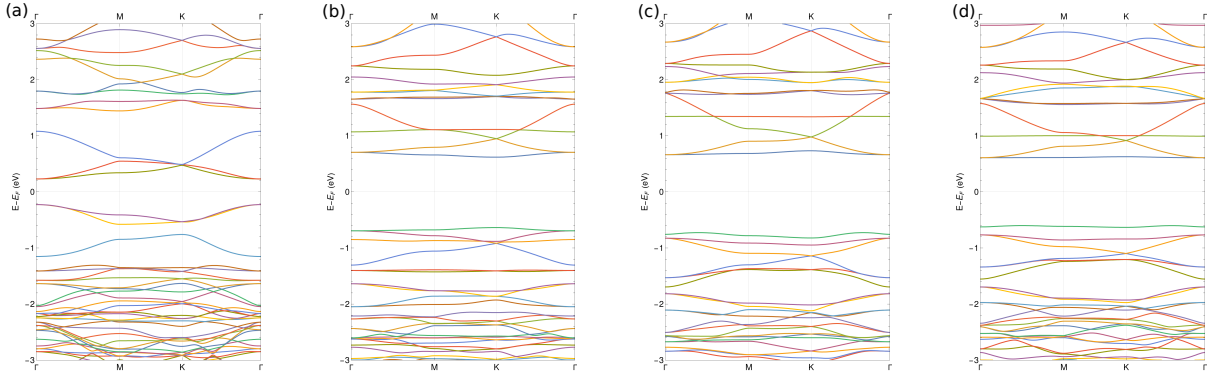
Figure 4.8: r^2SCAN+rvv10 computed bands for the different 6×6 FLD superlattices: (a) 6×6-FLD, (b) 6×6-FLD-12h, (c) 6×6-FLD-12hud, and (d) 6×6-FLD-12hudu. Note the aperture on the bandgap on the structures with H adatoms.

expectations, no bandgap was observed in these alternative structures as reported in Table 4.2, diverging from the results obtained for the 6×6 H configurations.

Table 4.2: Structural and electronic r^2SCAN+rvv10 computed properties of 5×5 and 7×7 FLD superlattices with H adatoms on the edge. a_0 represents the optimal lattice parameter, E_g is the bandgap, N_C is the number of carbon atoms, N_H is the number of hydrogen adatoms, ΔE_c is the cohesive energy, γ_0 is the layer modulus, and Symmetry indicates the crystal symmetry.

System	a_0 (Å)	E_g (eV)	N_C	N_H	ΔE_c(eV/atom)	γ_0 (N m^{-1})	Symmetry
Pristine	2.4535	0	2	0	-7.493	216.96	$P6/mmm$ (191)
5×5-FLD-12h	12.357	0	50	12	-4.262	116.49	$P6mm$ (183)
5×5-FLD-12hud	12.287	0	50	12	-4.283	105.01	$P3m1$ (156)
5×5-FLD-12hudu	12.484	0	50	12	-4.272	128.37	$P6$ (168)
7×7-FLD-12h	17.169	0	98	12	-6.523	111.04	$C1m1$ (8)
7×7-FLD-12hud	17.169	0	98	12	-6.536	108.16	$P1$ (1)
7×7-FLD-12hudu	17.349	0	98	12	-6.527	157.49	$P121$ (3)

An interesting observation was found from Table 4.2, the results of the layer modulus, γ_0 for the 12hudu configurations in the 5×5 and 7×7 superlattices present the higher values indicating superior mechanical strength compared with the other configurations, similar trend is observed for the 6×6 cases (cf. Table 4.1)

Regarding the band structure of the 5×5 FLD superlattices, the band structures shown in Fig. 4.11 exhibit a similar features around the Fermi level where is observed two bands with small dispersion. According to their respective PDOS illustrated in Figs. A.10-A.15, these states near the Fermi level are predominantly contributed by
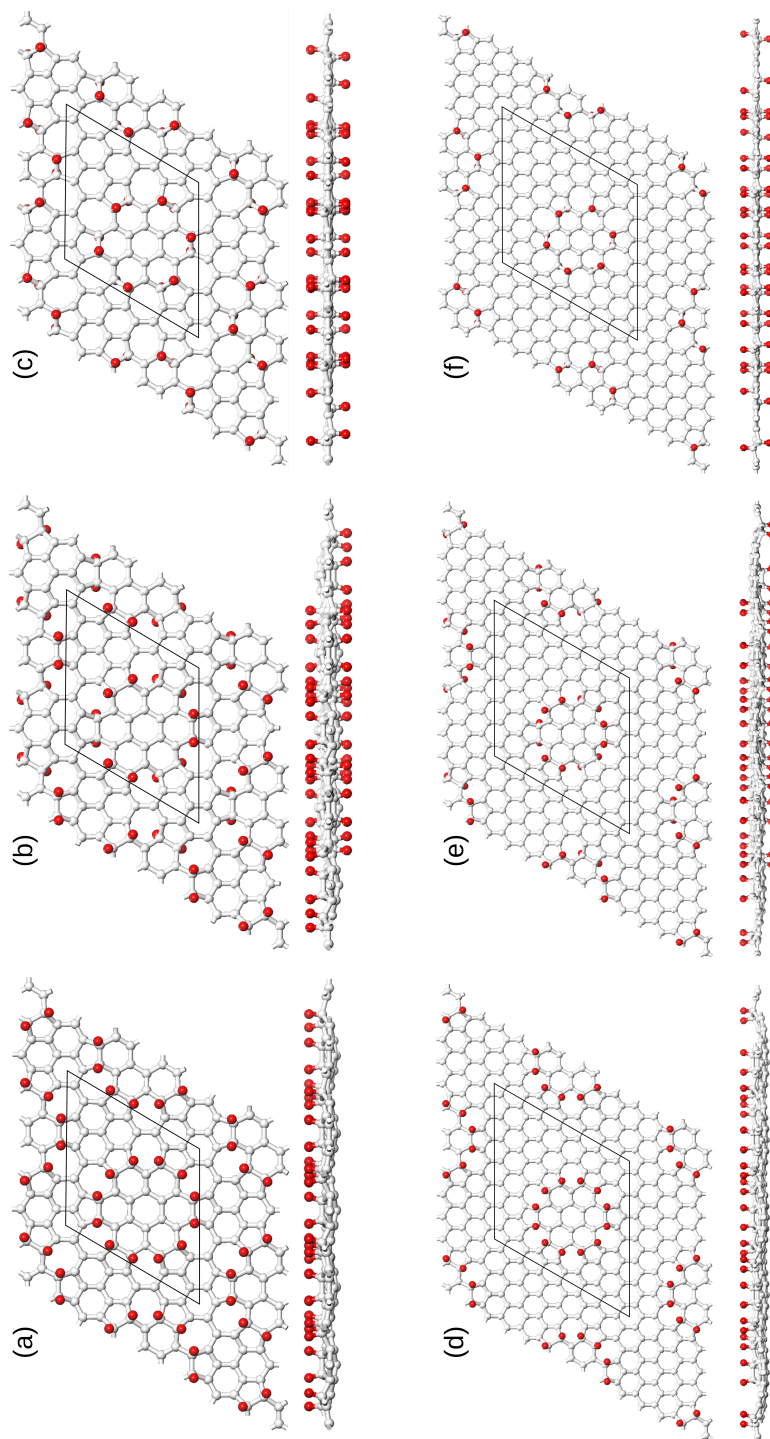
Figure 4.9: (a,d) Configuration for 5×5 and 7×7 FLD-12hud, where all H adatoms have the same orientation. (b,e) Configuration 5×5 and 7×7 FLD-12hud, with two H adatoms oriented upward, followed by the next two oriented downward. (c,f) Configuration 5×5 and 7×7 FLD-12hudu involves alternating H adatoms between upward and downward orientations.

the *2pz* orbitals of the C atoms outside of the FLD, with a minor contribution from the 1*s* states of the H adatoms.

The 5×5 FLD superlattices with H adatoms are a special case since the structure consists of 50 carbon atoms, with 24 C atoms forming the FLD and 26 non-deformed C atoms accompanied by 12 H adatoms. This configuration appears to be more likely an allotrope of graphene, which could be the reason why its electronic structure (Fig. 4.11) and layer modulus values significantly differ from the other superlattices and pristine graphene.
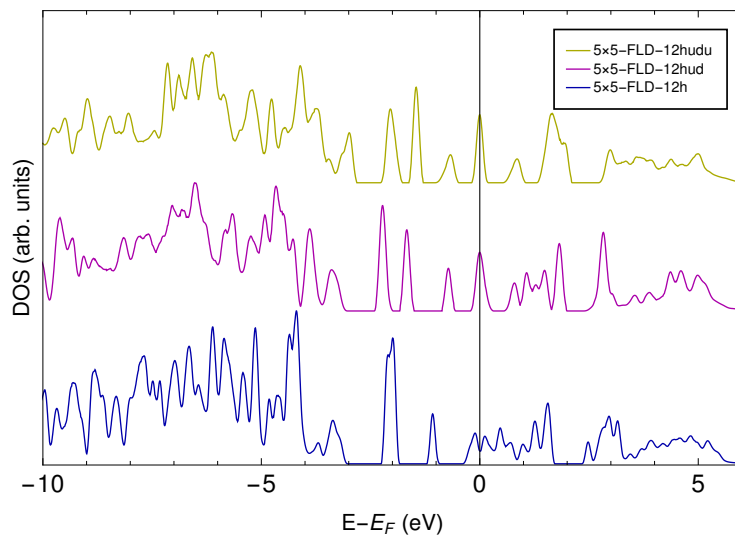
Figure 4.10: r^{2}SCAN+rVV10 computed DOS for the different 5×5 superlattices with H adatoms configurations on the FLD's Edge.

For the 7×7 FLD superlattices with H adatoms, Fig. 4.13 reveals two distinct states near the Fermi level exhibiting linear dispersion, particularly around the K point. This observation is particularly important as it suggests the presence of Dirac cones in these structures. Further analysis, as depicted in Figs. A.16-A.21, indicates that near the Fermi level, the *2pz* states of primarily the C atoms at the outer edges of the FLD contribute to the formation of these cones. The advantage of these superlattices lies in their relatively higher cohesion energies compared to both the 5×5 and 6×6 FLD superlattices with H adatoms. The increased cohesion energy as illustrated in Table. 4.2 was expected due to the presence of more carbon atoms outside of the FLD, which means more C-C covalent bonds, i.e., stronger interatomic interactions within the superlattice structure.
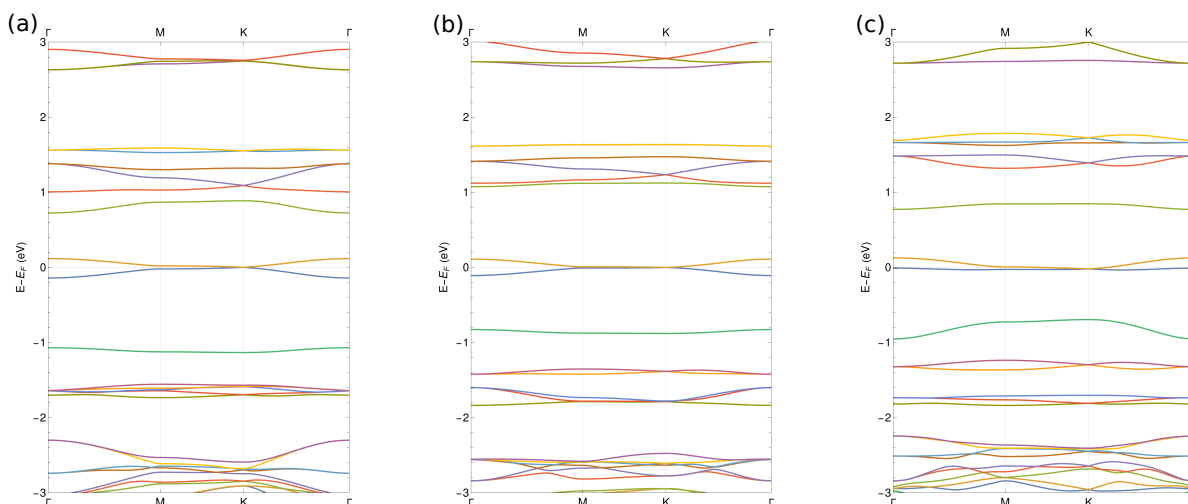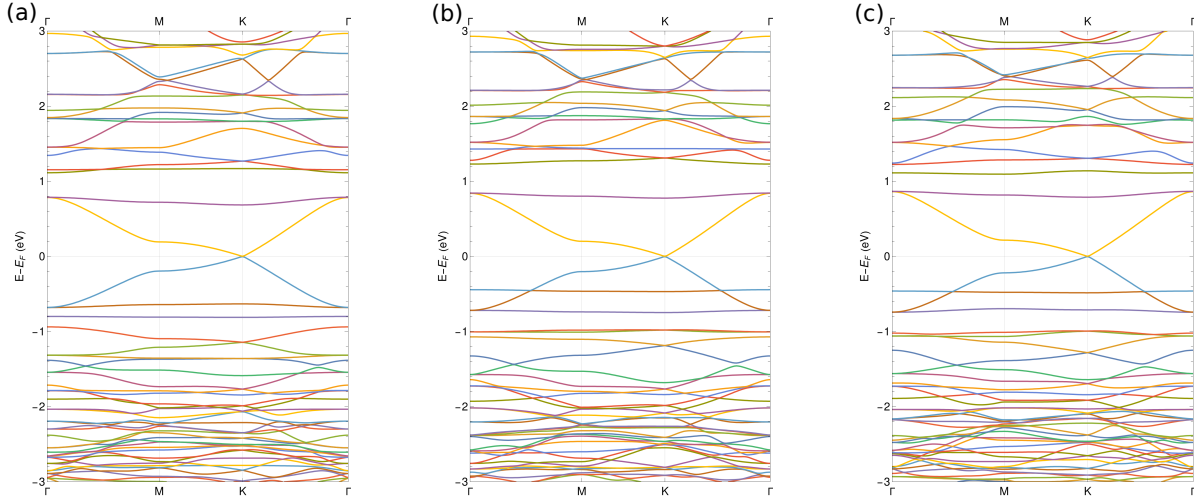
Figure 4.11: r²SCAN+rVV10 computed bands for the different 5×5 FLD superlattices: (a) 5×5-FLD-12h, (b) 5×5-FLD-12hud, and (c) 5×5-FLD-12hudu.
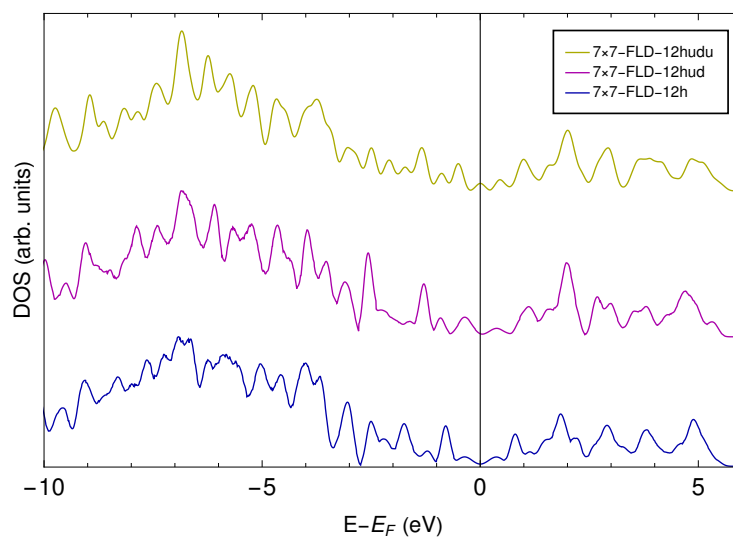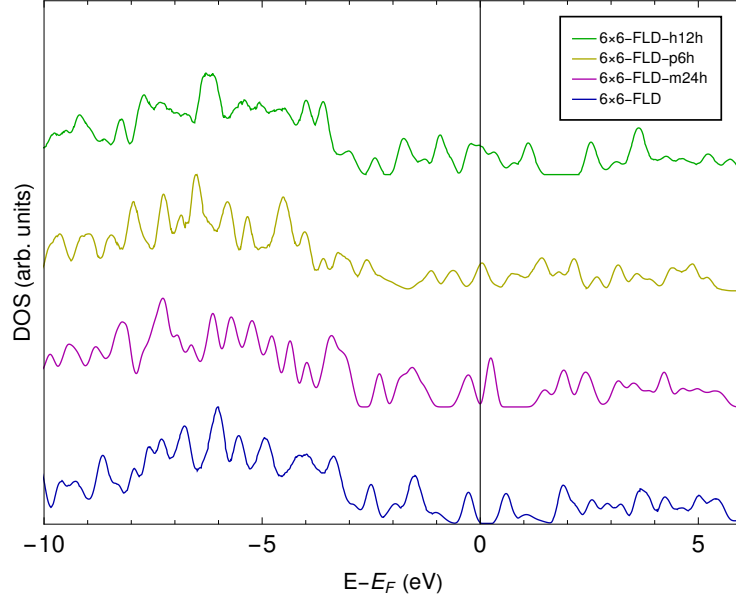

Figure 4.12: r²SCAN+rVV10 computed DOS for the different 7×7 superlattices with H adatoms configurations on the FLD's Edge.

The absence of a bandgap in both 5×5 and 7×7 superlattices, despite incorporating hydrogen adatoms, underscores the critical role of lattice size and symmetry in dictating electronic properties. This observation suggests that the influence of hydrogenation on bandgap engineering is not merely a function of adatom incorporation but also heavily

Figure 4.13: r^2SCAN+rVV10 computed bands for the different 7×7 FLD superlattices: (a) 7×7-FLD-12h, (b) 7×7-FLD-12hud, and (c) 7×7-FLD-12hudu.

depends on the geometric and electronic congruity of the underlying graphene lattice. Therefore, the variation in electronic properties with changing superlattice dimensions underscores the complex relationship between structural modifications and the electronic band structure, adding layers of complexity to the design of graphene-based electronic devices.

4.2.2   H Adatoms on the FLD's Inner & Outer Edge

In the region highlighted by the blue atoms in Figure 4.2, we examined three distinct configurations involving H placement. The first configuration, denoted as 6×6-FLD-m24h (4.14(a)), is based on Balog's concept[52], where H adatoms are arranged to create a moiré pattern, placing adatoms at the inner region and outer edge of the FLD. The second configuration, labeled as 6×6-FLD-h12h (4.14(b)), features H adatoms situated at the outer atoms of the heptagons, with a uniform orientation. The third configuration, called 6×6-FLD-p6h (4.14(c)), involves positioning H adatoms at the corner atoms of pentagons, all oriented in the same direction.
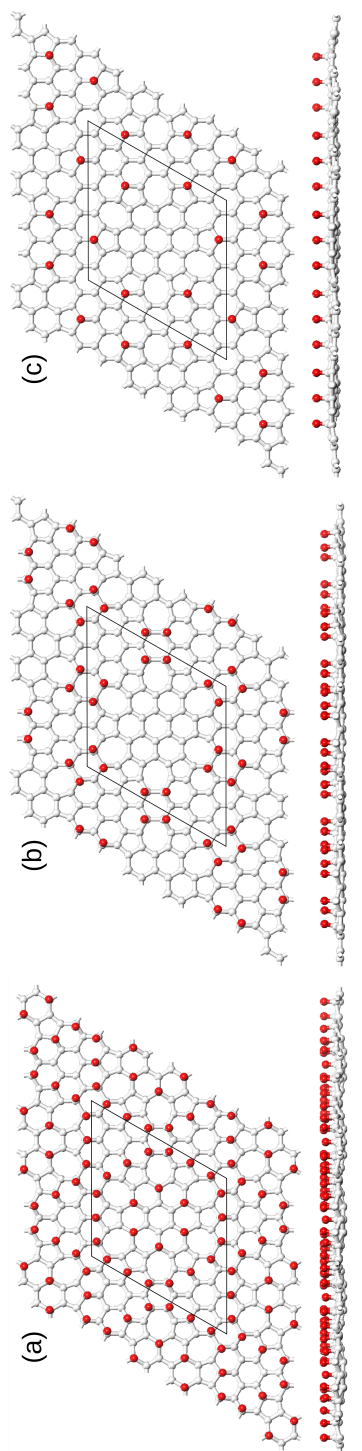
Figure 4.14: (a) Configuration 6×6-FLD-m24h, where all H adatoms create a Moiré pattern, and they have the same orientation. (b) Configuration 6×6-FLD-h12h, with the H adatoms situated at the outer atoms of the heptagons, also with a uniform orientation. (c) Configuration 6×6-FLD-p6h, involving H adatoms at the corner atoms of pentagons, all oriented in the same direction.

Figure 4.15: r^{2}SCAN+rVV10 computed DOS for the different 6×6 FLD superlattices with H adatoms configurations on the FLD's Inner & Outer Edge.

Table 4.3: r^{2}SCAN+rVV10 computed lattice parameters and energies of pristine graphene, 6×6 pristine graphene, 6×6-FLD superlattice, and 6×6-FLD superlattices with H adatoms at different configurations. a_0 is the optimum separation, N_C and N_H represent the number of C and H atoms, respectively. E_c is the cohesive energy per atom, and E_g represents the bandgap.

System	a_0 (Å)	E_g (eV)	N_C	N_H	ΔE_c(eV/atom)	γ_0 (N m^{-1})	Symmetry
6×6-FLD	14.817	0.63	72	0	-7.386	195.72	*P6mm* (183)
6×6-FLD-m24h	14.974	0.10	72	24	-6.051	135.94	*P6mm* (183)
6×6-FLD-p6h	14.830	0	72	6	-6.700	159.11	*Cmm*2 (35)
6×6-FLD-h12h	14.940	0	72	12	-6.146	182.26	*P*1 (1)

The exploration of H adatom configurations on the inner and outer edges of the FLD superlattices gives us an idea of the interplay between atomic modifications and electronic properties in graphene. The distinct configurations, namely 6×6-FLD-m24h, 6×6-FLD-h12h, and 6×6-FLD-p6h, not only serve as a testament to the versatility of graphene's electronic structure but also shed light on the sensitivity of graphene's electronic properties to precise atomic arrangements.
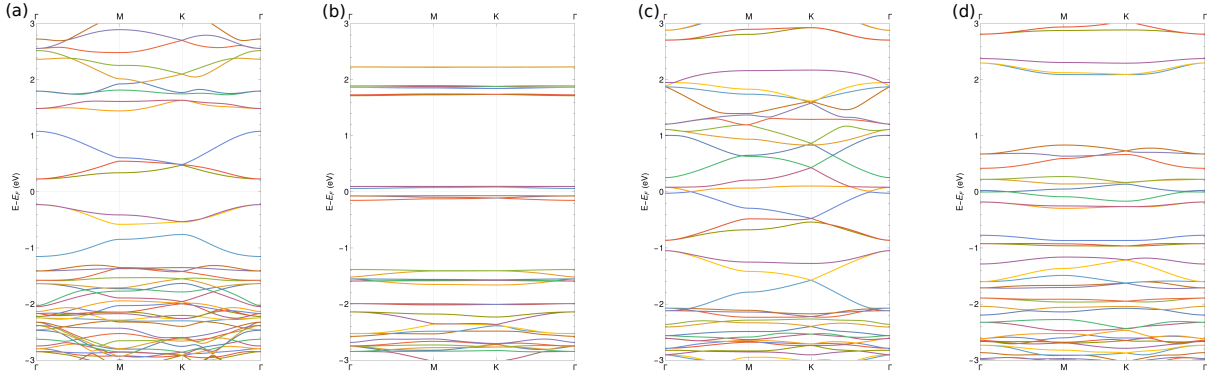
Figure 4.16: r^2SCAN+rVV10 computed bands for the different 6×6 FLD superlattices: (a) 6×6-FLD, (b) 6×6-FLD-m24h, (c) 6×6-FLD-p6h, and (d) 6×6-FLD-h12h.

4.3 Magnetic properties

The study of graphene's magnetic properties was inspired by Lehtinen *et al.*'s work[53], specifically the vacancy-induced magnetism in the graphene part. Considering that work, we aim to replicate their results and extend the exploration to graphene-based superlattices incorporating the FLD.

Table 4.4: Computed r^2SCAN+rvv10 properties of 6×6 superlattices with one C vacancy.

System	a_0 (Å)	E_g (eV)	N_C	N_H	ΔE_c(eV/atom)	γ_0 (N m^{-1})	μ_m (μ_β)	Symmetry
Pristine	2.453	0	2	0	-7.493	216.96	0	$P6/mmm$ (191)
6×6-pristine-1C$_V$	14.721	0.20	71	0	-7.375	-	2.00	P-6m2 (187)
6×6-FLD-1C$_V$	14.781	0	71	0	-7.280	162.832	1.14	$C1m$1 (8)

4.3.1 Vacancy-Induced Magnetism in Pristine Graphene

The process for studying this structure involved first constructing a 6×6 pristine supercell and subsequently removing one carbon atom from the superlattice, which we refer to as 6×6-pristine-1C$_V$ in Table 4.4. It is important to note that, in this particular case, we only allowed relaxation of the internal coordinates of the structure, while keeping the lattice parameter fixed. This approach was chosen because the vacancy is not anticipated to interact with its periodic image. Consequently, we were unable to calculate the layer modulus γ_0 in Table 4.4.

Additionally, to capture the magnetic properties, we used spin-polarized calculations in VASP. As a result, all the output files contain information related to the spin states. For instance, the DOSCAR file includes the density of states for different spins, while the OSZICAR and OUTCAR files provide details about the total magnetization and also the magnetization contributed by individual atoms.

Further analysis of Table 4.4 reveals some effects: the bandgap exhibits a tendency to open, and the formation energy is lower than pristine graphene as expected; our findings also indicate that the resultant ground state structure is magnetic, in agreement with the work of Lehtinen *et al.* [53]. However, while their report cites a magnetic moment of 1.04 μ_B, our results show 2.00 μ_B, as documented in Table 4.4.

Moreover, Figs. 4.17 and 4.18(a) illustrate the spin polarization effects induced by the vacancy. In particular, Fig. 4.17 shows the spin-resolved partial density of states (PDOS), where the spin-up states are represented by positive values in states/eV, and spin-down states are represented by negative values in states/eV. Additionally, Fig. 4.18(a) displays the distribution of spin-resolved magnetization density, further highlighting the vacancy's effect on the system's magnetic properties.

The work of Lehtinen *et al.* [53] explains that when a carbon ion is removed from a graphene lattice, it creates three unsaturated sp^2 orbitals in the neighboring carbon ions. The formation of a pentagon structure in the lattice saturates two of these orbitals, leaving one sp^2 orbital free. This remaining dangling bond contributes to the calculated localized magnetic moment, as illustrated in the Fig. 4.18(a).
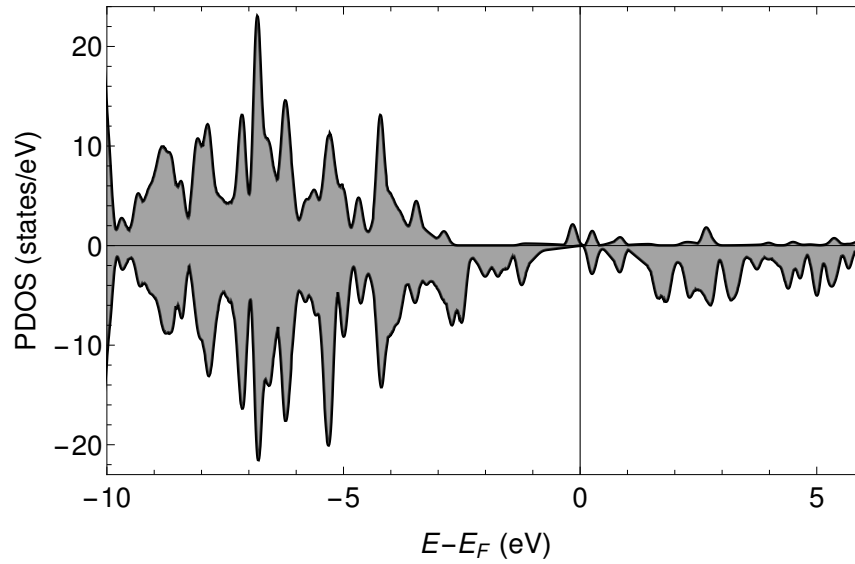
Figure 4.17: r^{2}SCAN+rvv10 spin-resolved PDOS of 6×6 graphene supercell with a carbon vacancy. The diagram delineates the PDOS with distinct curves for spin-up and spin-down states, illustrating the vacancy-induced spin polarization.

4.3.2   6×6-FLD with 1 C Vacancy

The investigation of this structure followed a similar procedure, with the addition of the FLD. Specifically, we constructed a 6×6 supercell, introduced a defect, and removed one carbon atom from the superlattice. This structure is called 6×6-FLD-1C_V, as shown in Table 4.4. After lattice and structural relaxation, we were able to apply the 2D
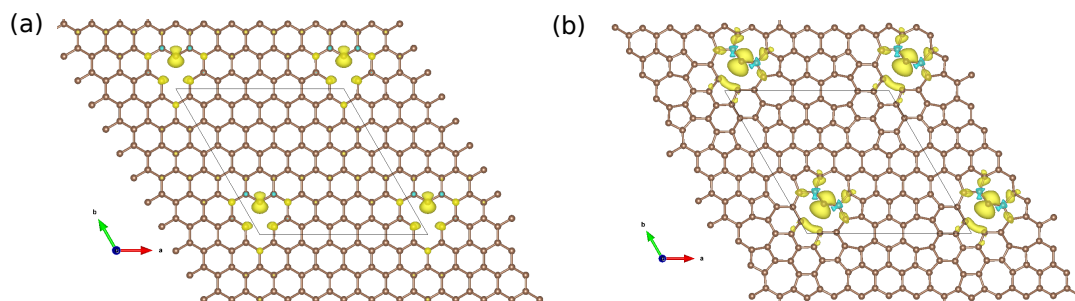
Figure 4.18: r^2SCAN+rvv10 spin-resolved magnetization density for (a) 6×6-pristine-1C$_V$ and (b) 6×6-FLD-1C$_V$. Note that yellow (cyan) represents positive (negative) magnetization density.

equation of state (EOS) and obtain the layer modulus γ_0 of the optimal structure, which resulted in 162.832 Nm^{-1}, as presented in Table 4.4.

Further examination of Table 4.4 reveals several effects: the bandgap observed in the 6×6-FLD structure vanishes, and the formation energy is lower than that of 6×6-FLD, consistent with expectations. Furthermore, our analysis confirms the magnetic nature of the resulting ground state structure. The magnetic moment is quantified at 1.14 μ_B, as detailed in Table 4.4. Fig. 4.19 highlights the spin polarization effects induced by the vacancy. Specifically, Fig. 4.19 presents the spin-resolved PDOS, distinguishing the contributions from carbon atoms inside and outside the FLD. Furthermore, the lack of enhanced magnetic properties in this structure, compared to pristine graphene with a single vacancy, could be due to the suboptimal positioning of the vacancy within the flower-like region, which may not be conducive to achieving the desired magnetic enhancement.

Aditionally, it is crucial to approach these results with caution. Kothakonda *et al.*[28] compared SCAN, r^2SCAN and GGA-PBE. They found that PBE provides more accurate results than the more sophisticated meta-GGAs for determining the magnetic moments of metals; nonetheless, in the same study, it is recommended the use of r^2SCAN+rvv10 for layered materials, which applies to graphene.
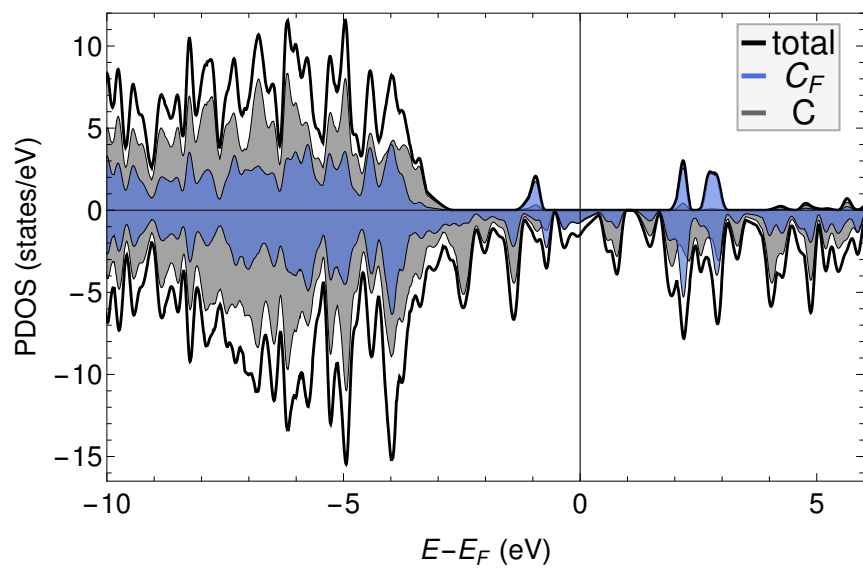
Figure 4.19: r^{2}SCAN+rvv10 spin-resolved PDOS of 6×6-FLD-1C$_V$ structure, illustrating the differentiated electronic contributions from C atoms located within and outside the FLD.

Chapter 5

Conclusions & Outlook

The first part of this work focused on exploring the FLD and adding H adatoms within graphene superlattices. Specifically, we studied the 5×5, 6×6, and 7×7 configurations to uncover potential alterations in their electronic structures. Various H configurations were examined across these superlattices using DFT calculations performed through the VASP and employing the r^2SCAN+rVV10 functional. After each structure's lattice and structural relaxation, an equation of state tailored for two-dimensional systems was applied to obtain the ground-state energy configurations along with their distinctive electronic structures.

The density of states and band structures for all optimal superlattices were computed for a comprehensive analysis. Moreover, STM simulations were calculated for structures with a band gap opening, enhancing our understanding of their electronic properties.

Our results showed that placing three H adatoms at the edges of the FLD in the 6×6 superlattice increased the bandgap beyond that of the superlattice without H adatoms. This phenomenon led us to examine the same H configurations within 5×5 and 7×7 superlattices, investigating the effects of altering superlattice dimensions, which inherently modifies the spatial intervals between FLDs. We were aware of previous research by Garzón et al. [51], which proposed a "band gap opening rule" suggesting that superlattices with dimensions that are multiples of 3 exhibit a bandgap (e.g., 3×3, 6×6, 9×9, etc). We aimed to open a bandgap in those superlattices that did not exhibit one without H adatoms, such as the 5×5 and 7×7. However, our investigations revealed that these modifications failed to induce a bandgap in both 5×5 and 7×7 configurations, indicating that the impact of H adatoms on the bandgap is not only dependent on adatom incorporation but also significantly influenced by the geometric and electronic properties of the underlying graphene lattice.

Then, further investigations into the 6×6 superlattice, with H adatoms strategically placed both external and internal to the FLD, were performed. These alternative configurations did not facilitate bandgap expansion; instead, they closed the bandgap that the superlattice without H adatoms had. This observation elucidates that the external placement of H adatoms around the FLD tends to narrow the bandgap.

The second part of this work investigated the magnetic properties of pristine graphene and graphene with an FLD by introducing a single carbon vacancy in a 6×6 supercell. For pristine graphene, the magnetic moment of the

resulting ground state structure was 2.00 μ_B, higher than the 1.04 μ_B reported by Lehtinen *et al.* On the other hand, the 6×6-FLD ground state structure was found to be magnetic with a magnetic moment of 1.14 μ_B, showing that the vacancy does not enhance the magnetic properties compared to pristine graphene with a single vacancy.

This overall analysis underscores the critical impact of precise atomic-level modifications on the properties of graphene with the FLD, emphasizing the necessity of detailed structural characterization in developing graphene-based materials. Future research related to the band gap manipulation could extend these findings by investigating the influence of varying H patterns and coverage and introducing different adatom species, such as transition metals. To enhance the magnetic properties, investigating different arrangements of vacancies within the FLD structure and adding adatoms could offer valuable insights into optimizing these properties.

Appendix A

```
C : graphene 1x1v15
   1.00000000000000
     2.1247964181637609    -1.2267517840000000     0.0000000000000000
     0.0000000000000000     2.4535035679999999     0.0000000000000000
     0.0000000000000000     0.0000000000000000    15.0000000000000000
   C
     2
Selective dynamics
Direct
  0.3333333333333925   0.6666666666669698   0.0277777777777786   T   T   T
  0.6666666666665080   0.3333333333333925   0.0277777777777786   T   T   T
```
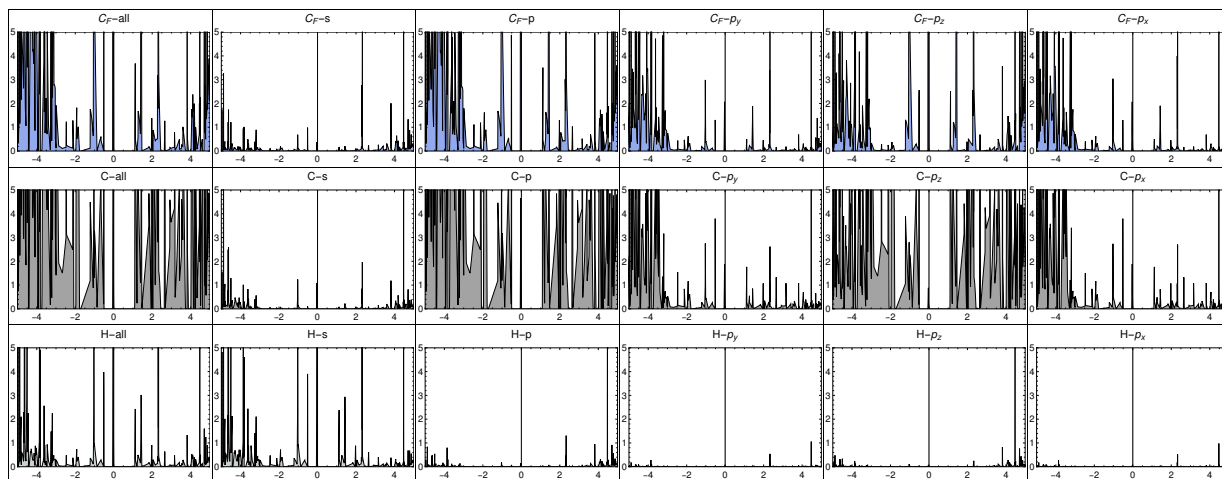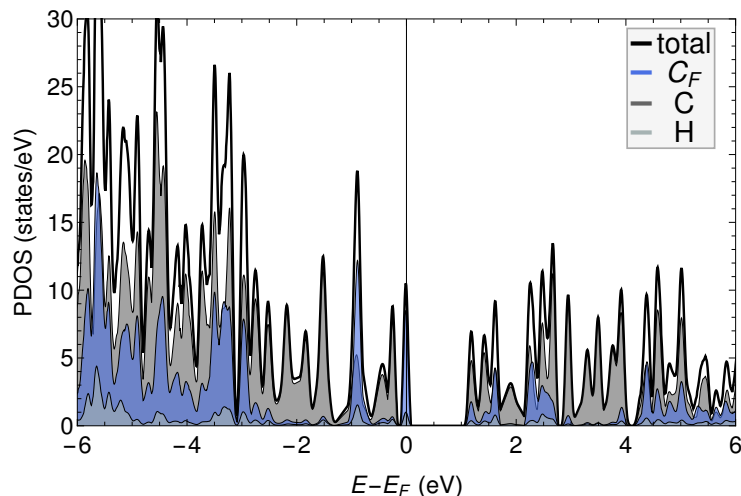
Figure A.1: Pristine Graphene POSCAR File
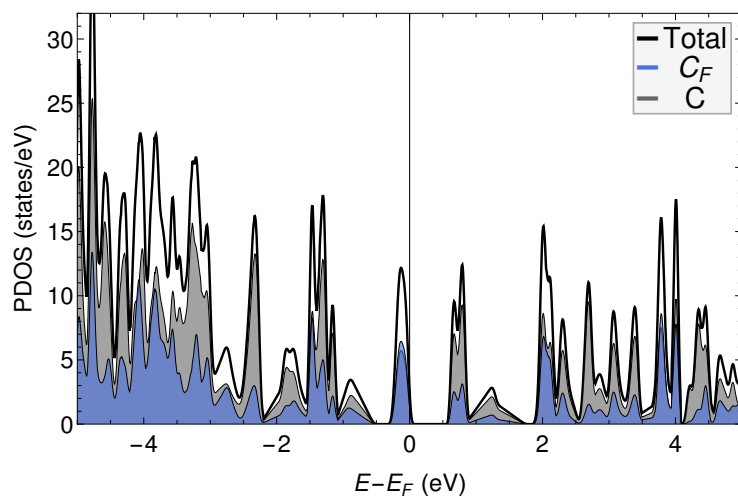
Figure A.2: 6×6-FLD Partial Density of States (PDOS), highlighting the distinct electronic states contributed by different types of atoms. Here, C_F denotes the carbon atoms constituting the FLD structure within the lattice and C represents the carbon atoms outside of the FLD. The Fermi level is centered at zero.
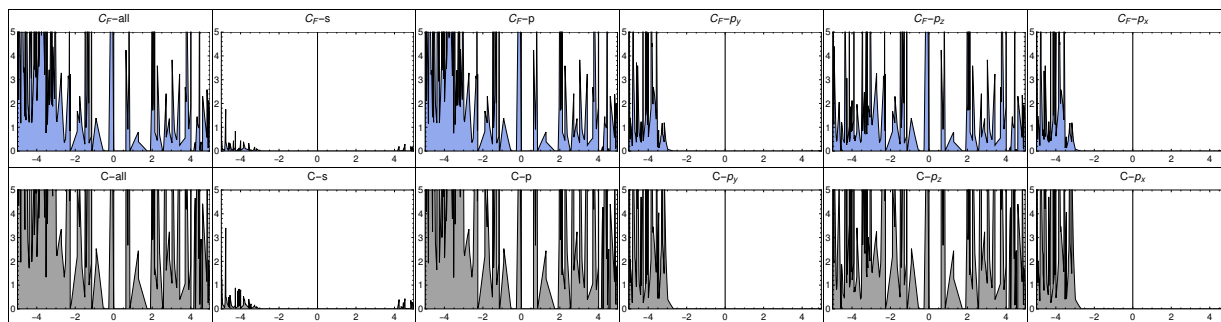
Figure A.3: 6×6-FLD detailed atomic orbital PDOS, showcasing the distinct contributions of each atomic orbital to the overall electronic states.
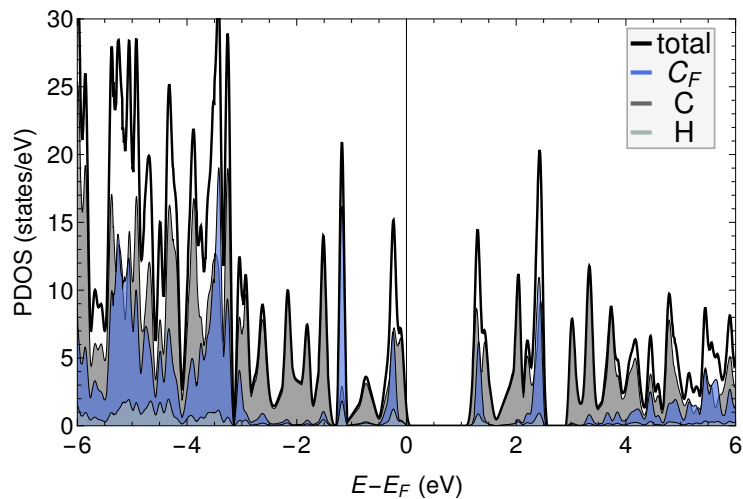
Figure A.4: 6×6-FLD-12h Partial Density of States (PDOS), highlighting the distinct electronic states contributed by different types of atoms. Here, C_F denotes the carbon atoms constituting the FLD structure within the lattice and C represents the carbon atoms outside of the FLD, and H refers to all the hydrogen (H) adatoms.
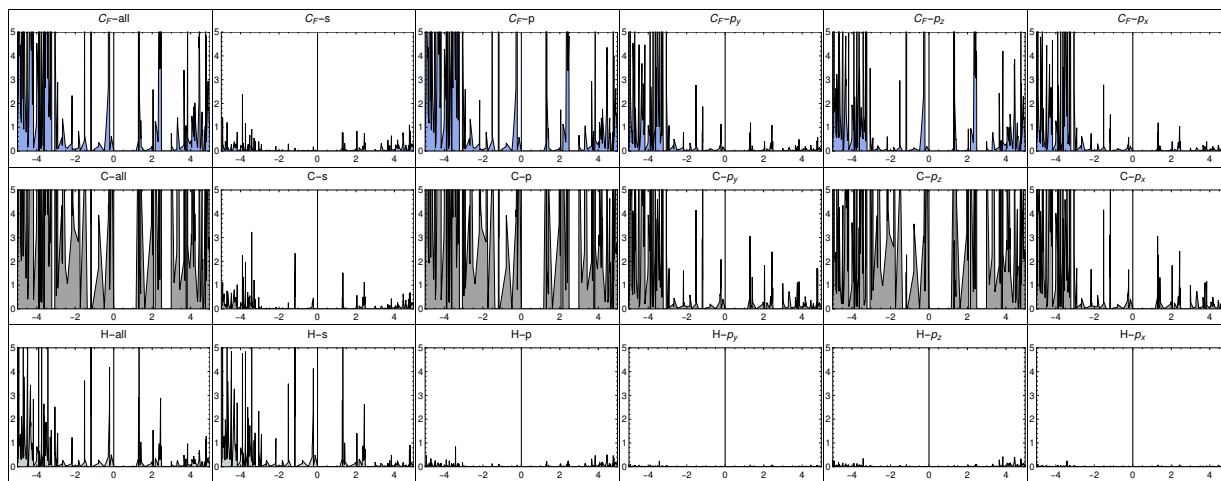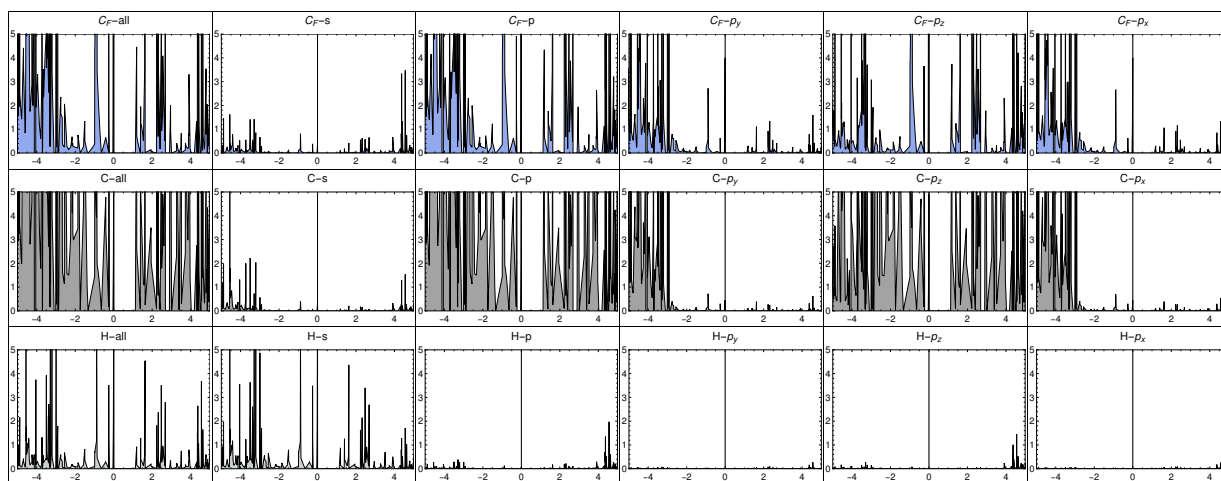

Figure A.5: 6×6-FLD-12h detailed atomic orbital PDOS, highlighting the distinct electronic states contributed by different types of atoms. Here, C_F denotes the carbon atoms constituting the FLD structure within the lattice and C represents the carbon atoms outside of the FLD, and H refers to all the hydrogen (H) adatoms.
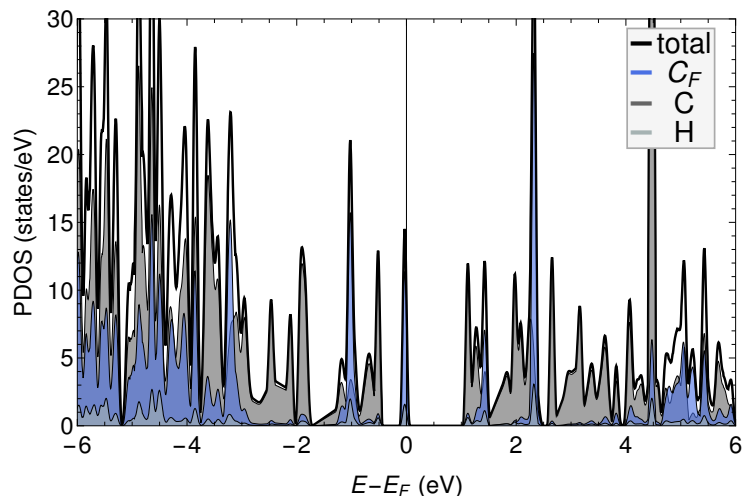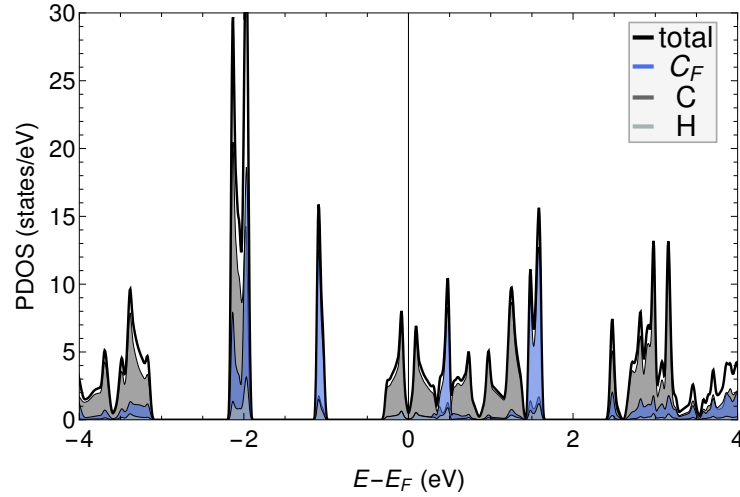
Figure A.6: 6×6-FLD-12hud Partial Density of States (PDOS), highlighting the distinct electronic states contributed by different types of atoms. Here, C_F denotes the carbon atoms constituting the FLD structure within the lattice and C represents the carbon atoms outside of the FLD, and H refers to all the hydrogen (H) adatoms.
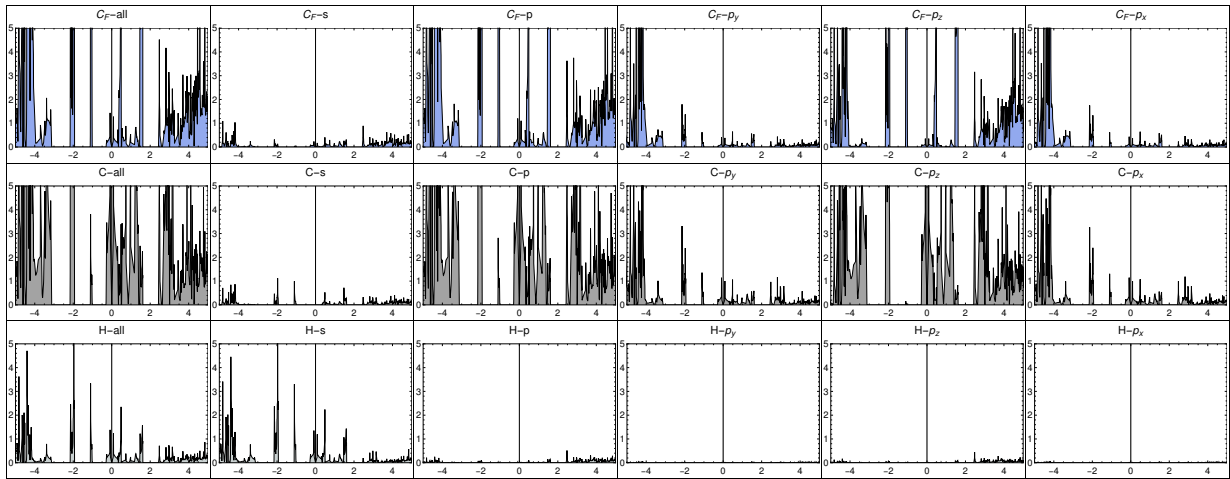

Figure A.7: 6×6-FLD-12hud detailed atomic orbital PDOS, highlighting the distinct electronic states contributed by different types of atoms. Here, C_F denotes the carbon atoms constituting the FLD structure within the lattice and C represents the carbon atoms outside of the FLD, and H refers to all the hydrogen (H) adatoms.

Figure A.8: 6×6-FLD-12hudu Partial Density of States (PDOS), highlighting the distinct electronic states contributed by different types of atoms. Here, C_F denotes the carbon atoms constituting the FLD structure within the lattice and C represents the carbon atoms outside of the FLD, and H refers to all the hydrogen (H) adatoms.
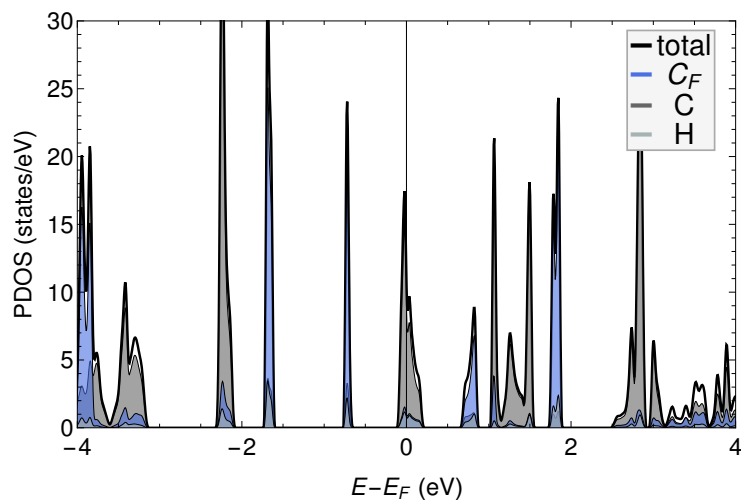

Figure A.9: 6×6-FLD-12hudu detailed atomic orbital PDOS, highlighting the distinct electronic states contributed by different types of atoms. Here, C_F denotes the carbon atoms constituting the FLD structure within the lattice and C represents the carbon atoms outside of the FLD, and H refers to all the hydrogen (H) adatoms.
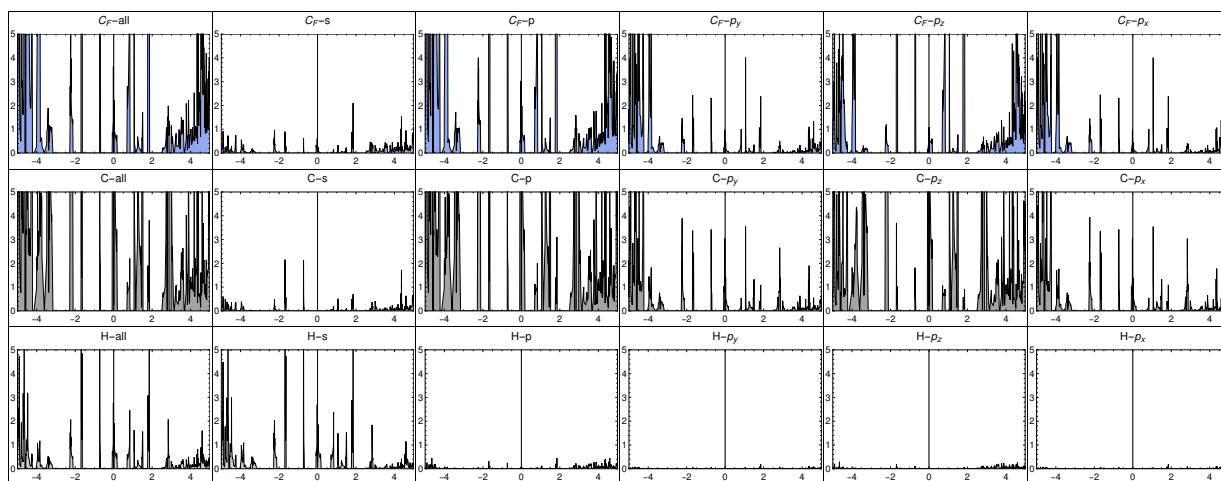
Figure A.10: 5×5-FLD-12h Partial Density of States (PDOS), highlighting the distinct electronic states contributed by different types of atoms. Here, C_F denotes the carbon atoms constituting the FLD structure within the lattice and C represents the carbon atoms outside of the FLD, and H refers to all the hydrogen (H) adatoms.
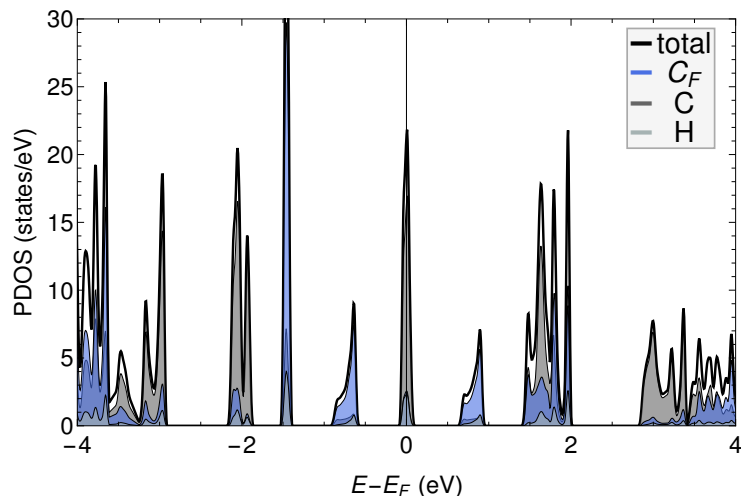

Figure A.11: 5×5-FLD-12h detailed atomic orbital PDOS, highlighting the distinct electronic states contributed by different types of atoms. Here, C_F denotes the carbon atoms constituting the FLD structure within the lattice and C represents the carbon atoms outside of the FLD, and H refers to all the hydrogen (H) adatoms.

Figure A.12: 5×5-FLD-12hud Partial Density of States (PDOS), highlighting the distinct electronic states contributed by different types of atoms. Here, C_F denotes the carbon atoms constituting the FLD structure within the lattice and C represents the carbon atoms outside of the FLD, and H refers to all the hydrogen (H) adatoms.
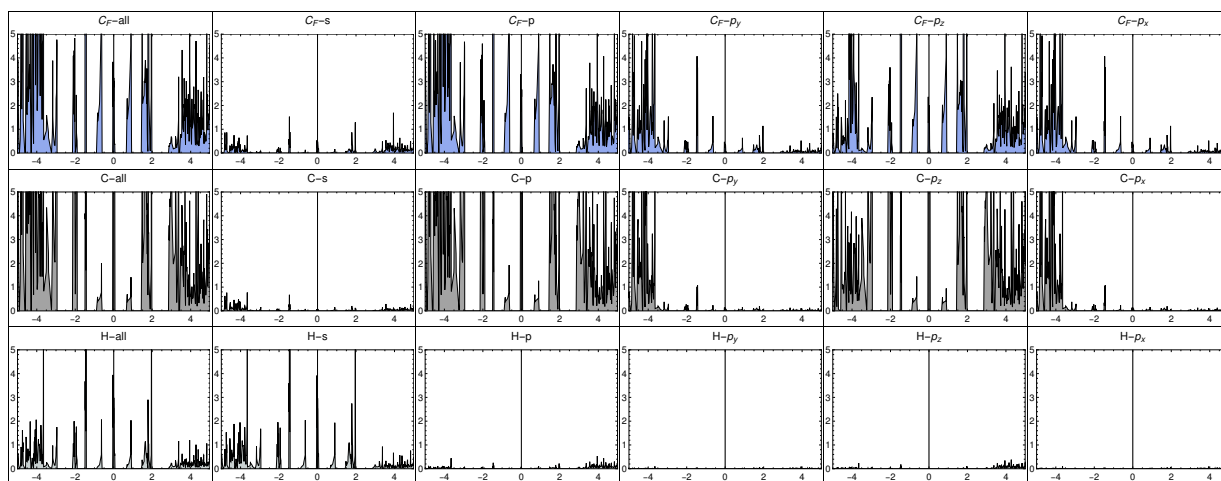

Figure A.13: 5×5-FLD-12hud detailed atomic orbital PDOS, highlighting the distinct electronic states contributed by different types of atoms. Here, C_F denotes the carbon atoms constituting the FLD structure within the lattice and C represents the carbon atoms outside of the FLD, and H refers to all the hydrogen (H) adatoms.
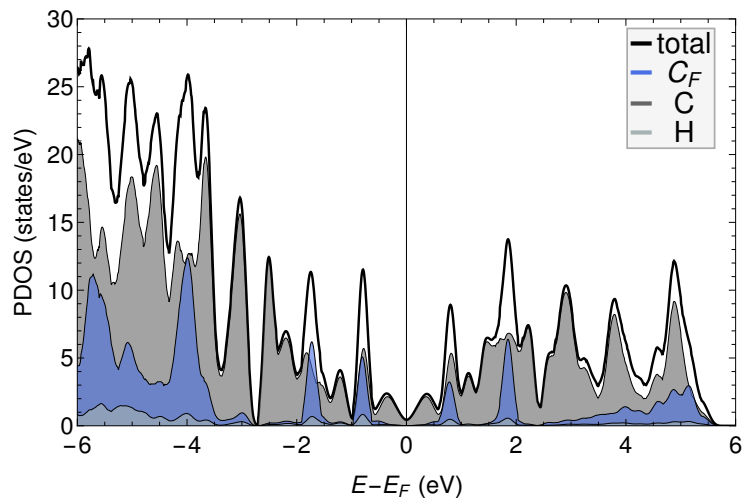
Figure A.14: 5×5-FLD-12hudu Partial Density of States (PDOS), highlighting the distinct electronic states contributed by different types of atoms. Here, C_F denotes the carbon atoms constituting the FLD structure within the lattice and C represents the carbon atoms outside of the FLD, and H refers to all the hydrogen (H) adatoms.
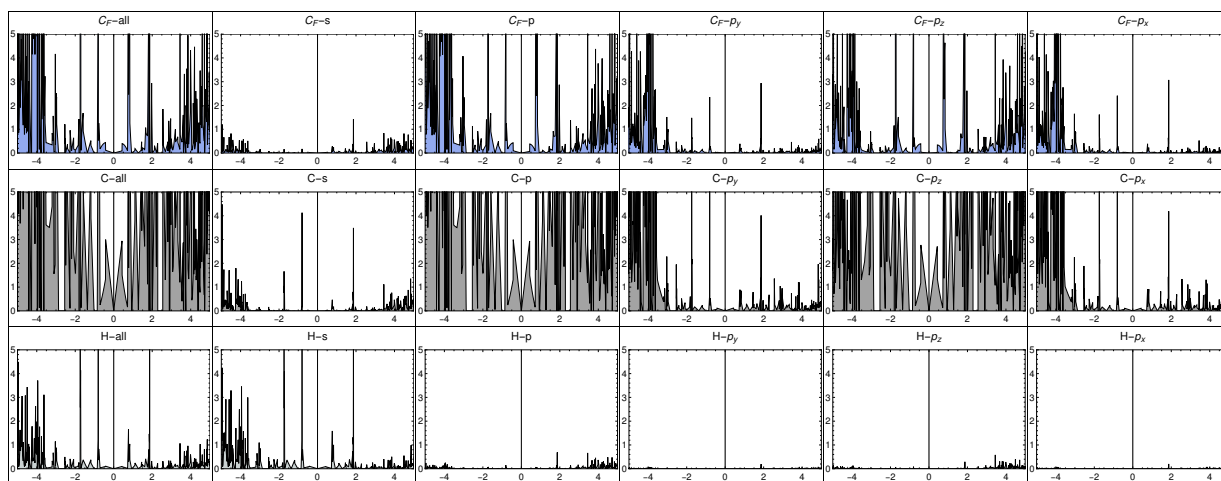

Figure A.15: 5×5-FLD-12hudu detailed atomic orbital PDOS, highlighting the distinct electronic states contributed by different types of atoms. Here, C_F denotes the carbon atoms constituting the FLD structure within the lattice and C represents the carbon atoms outside of the FLD, and H refers to all the hydrogen (H) adatoms.

Figure A.16: 7×7-FLD-12h Partial Density of States (PDOS), highlighting the distinct electronic states contributed by different types of atoms. Here, C_F denotes the carbon atoms constituting the FLD structure within the lattice and C represents the carbon atoms outside of the FLD, and H refers to all the hydrogen (H) adatoms.
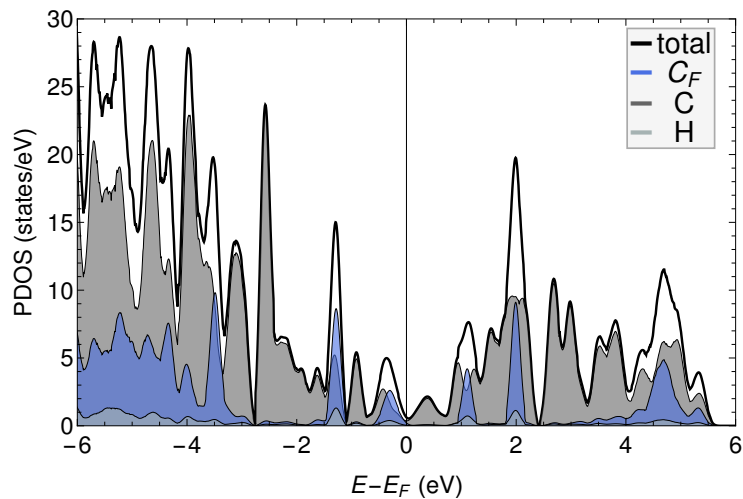

Figure A.17: 7×7-FLD-12h detailed atomic orbital PDOS, highlighting the distinct electronic states contributed by different types of atoms. Here, C_F denotes the carbon atoms constituting the FLD structure within the lattice and C represents the carbon atoms outside of the FLD, and H refers to all the hydrogen (H) adatoms.
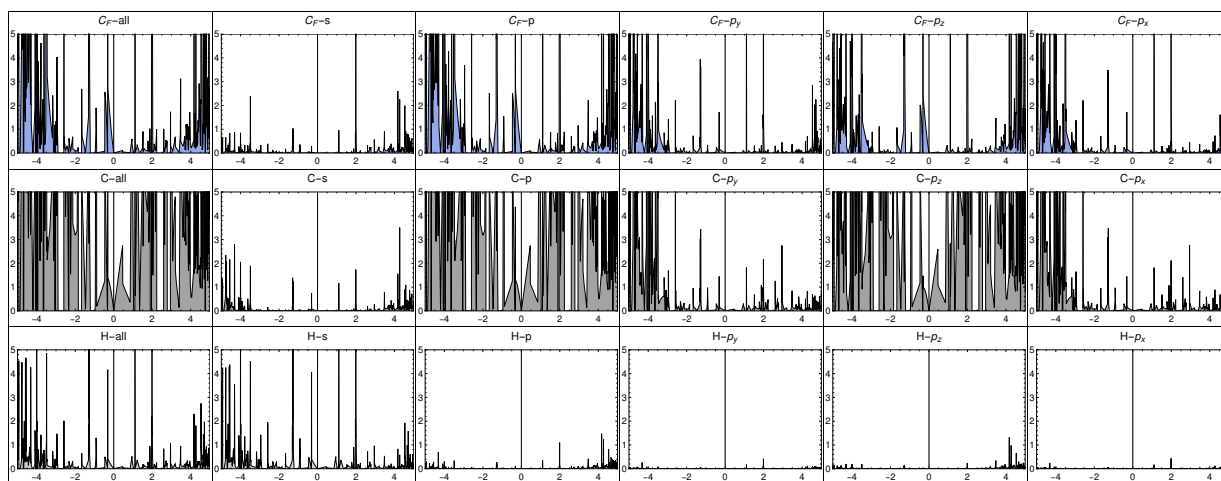
Figure A.18: 7×7-FLD-12hud Partial Density of States (PDOS), highlighting the distinct electronic states contributed by different types of atoms. Here, C_F denotes the carbon atoms constituting the FLD structure within the lattice and C represents the carbon atoms outside of the FLD, and H refers to all the hydrogen (H) adatoms.

Figure A.19: 7×7-FLD-12hud detailed atomic orbital PDOS, highlighting the distinct electronic states contributed by different types of atoms. Here, C_F denotes the carbon atoms constituting the FLD structure within the lattice and C represents the carbon atoms outside of the FLD, and H refers to all the hydrogen (H) adatoms.
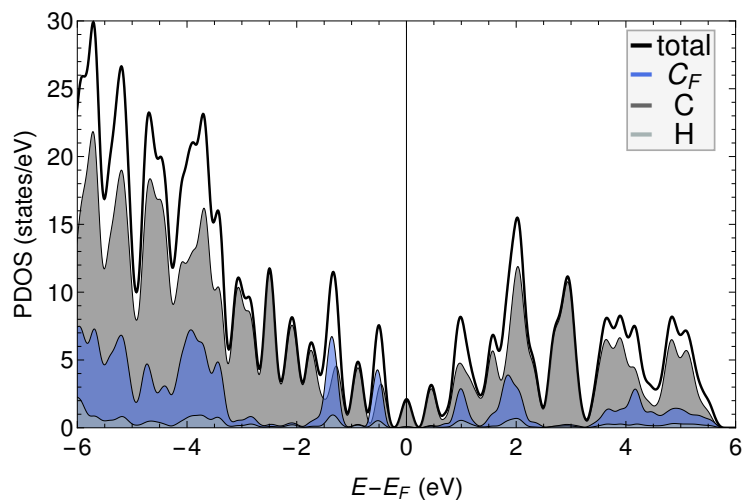
Figure A.20: 7×7-FLD-12hudu Partial Density of States (PDOS), highlighting the distinct electronic states contributed by different types of atoms. Here, C_F denotes the carbon atoms constituting the FLD structure within the lattice and C represents the carbon atoms outside of the FLD, and H refers to all the hydrogen (H) adatoms.
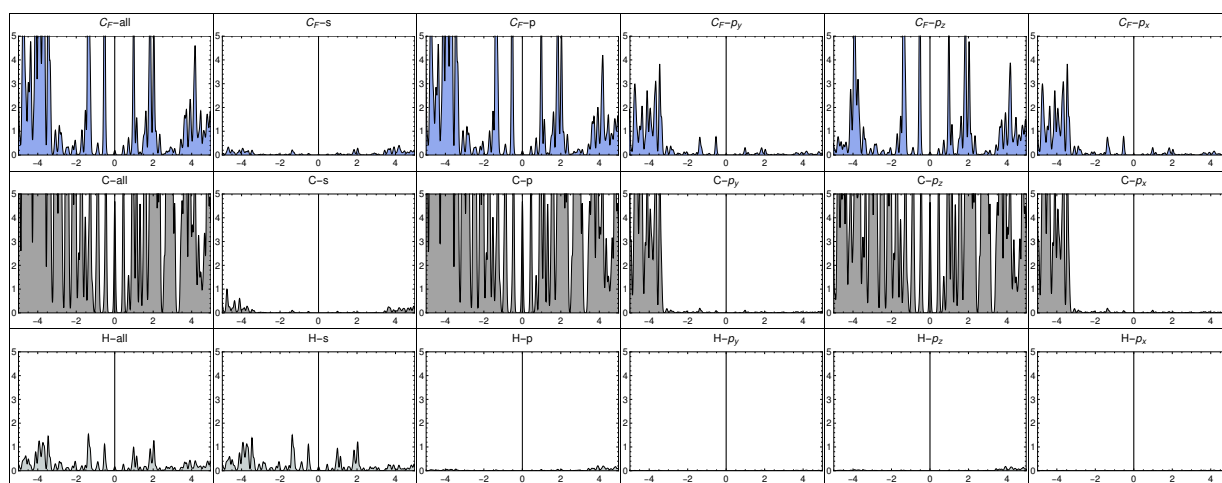

Figure A.21: 7×7-FLD-12hudu detailed atomic orbital PDOS, highlighting the distinct electronic states contributed by different types of atoms. Here, C_F denotes the carbon atoms constituting the FLD structure within the lattice and C represents the carbon atoms outside of the FLD, and H refers to all the hydrogen (H) adatoms.
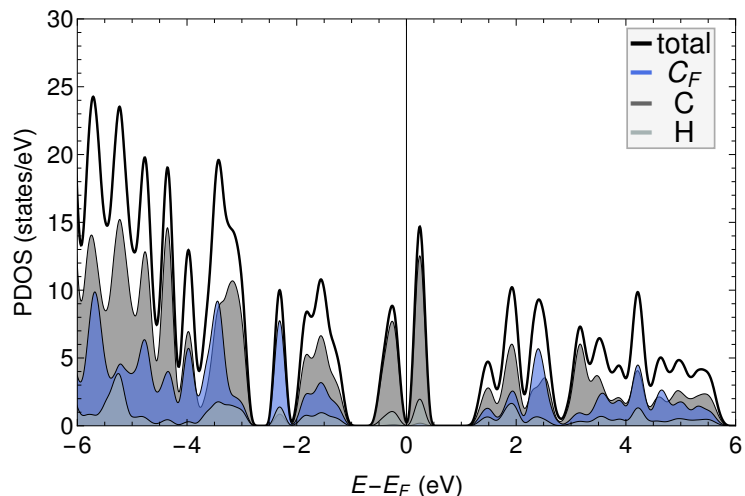
Figure A.22: 6×6-FLD-m24h Partial Density of States (PDOS), highlighting the distinct electronic states contributed by different types of atoms. Here, C_F denotes the carbon atoms constituting the FLD structure within the lattice and C represents the carbon atoms outside of the FLD, and H refers to all the hydrogen (H) adatoms.

Figure A.23: 6×6-FLD-m24h detailed atomic orbital PDOS, highlighting the distinct electronic states contributed by different types of atoms. Here, C_F denotes the carbon atoms constituting the FLD structure within the lattice and C represents the carbon atoms outside of the FLD, and H refers to all the hydrogen (H) adatoms.
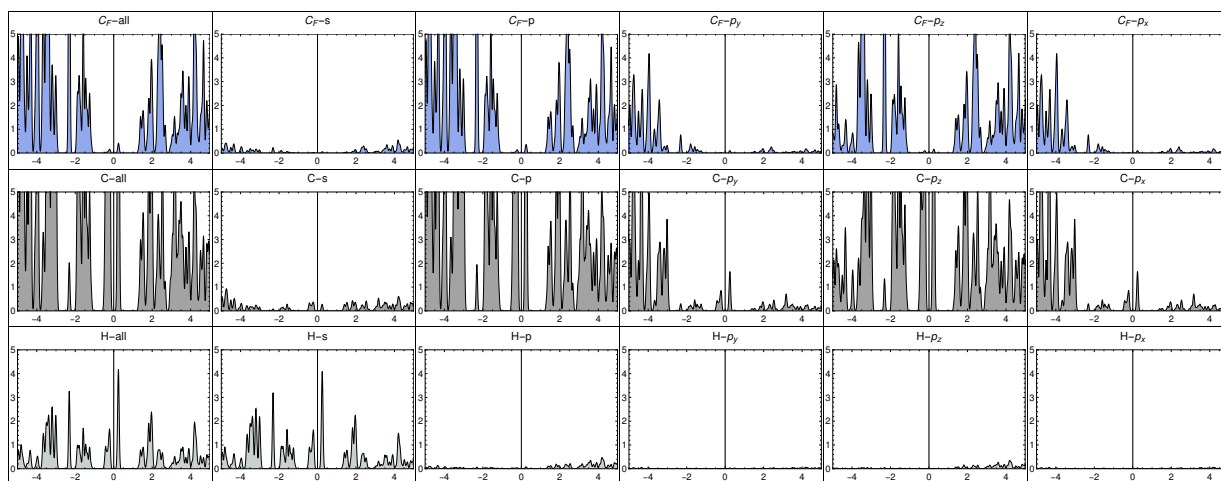
Figure A.24: 6×6-FLD-p6h Partial Density of States (PDOS), highlighting the distinct electronic states contributed by different types of atoms. Here, C_F denotes the carbon atoms constituting the FLD structure within the lattice and C represents the carbon atoms outside of the FLD, and H refers to all the hydrogen (H) adatoms.
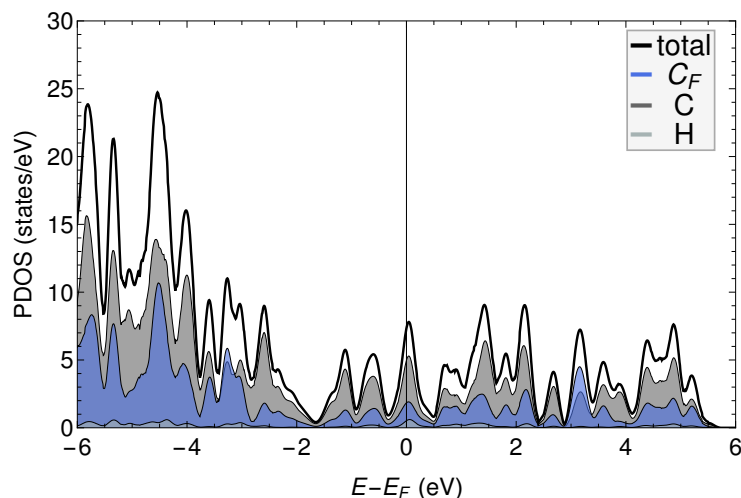

Figure A.25: 6×6-FLD-p6h detailed atomic orbital PDOS, highlighting the distinct electronic states contributed by different types of atoms. Here, C_F denotes the carbon atoms constituting the FLD structure within the lattice and C represents the carbon atoms outside of the FLD, and H refers to all the hydrogen (H) adatoms.
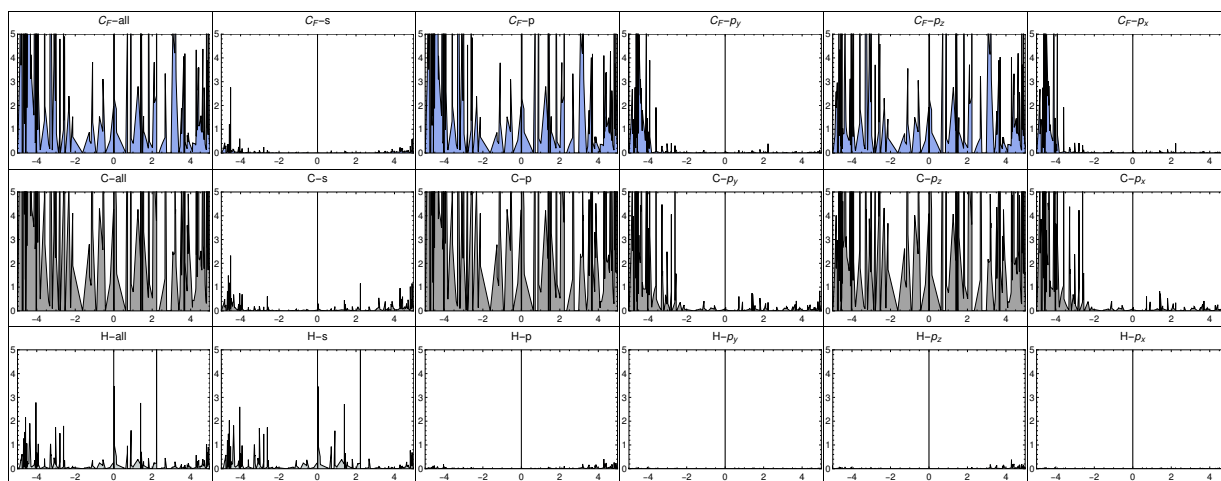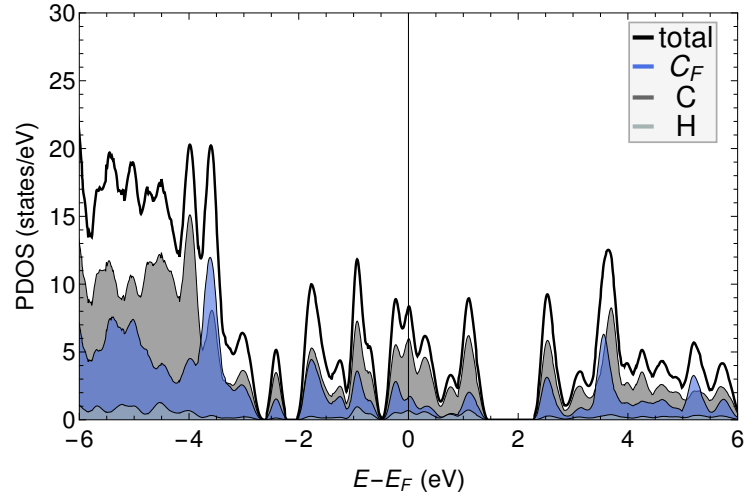
Figure A.26: 6×6-FLD-h12h Partial Density of States (PDOS), highlighting the distinct electronic states contributed by different types of atoms. Here, C_F denotes the carbon atoms constituting the FLD structure within the lattice and C represents the carbon atoms outside of the FLD, and H refers to all the hydrogen (H) adatoms.

Figure A.27: 6×6-FLD-h12h detailed atomic orbital PDOS, highlighting the distinct electronic states contributed by different types of atoms. Here, C_F denotes the carbon atoms constituting the FLD structure within the lattice and C represents the carbon atoms outside of the FLD, and H refers to all the hydrogen (H) adatoms.
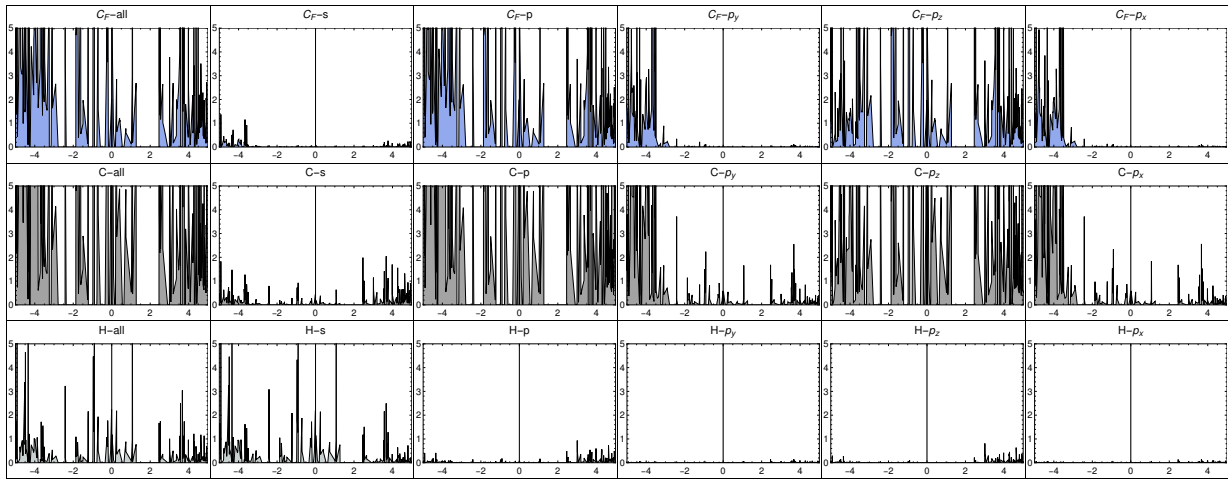
Bibliography

[1] Geim, A.; Novoselov, K. The rise of graphene. *Nature Materials* **2004**, *6*, 183–191.

[2] The Nobel Prize in Physics 2010 - NobelPrize.org. Accessed: 2023-10-21.

[3] Castro Neto, A. H.; Guinea, F.; Peres, N. M. R.; Novoselov, K. S.; Geim, A. K. The electronic properties of graphene. *Reviews of Modern Physics* **2009**, *81*, 109–162.

[4] Islam, M. A.; Serles, P.; Kumral, B.; Demingos, P. G.; Qureshi, T.; Meiyazhagan, A.; Puthirath, A. B.; Abdullah, M. S. B.; Faysal, S. R.; Ajayan, P. M. Exfoliation mechanisms of 2D materials and their applications. *Applied Physics Reviews* **2022**, *9*.

[5] Urade, A. R.; Lahiri, I.; Suresh, K. S. Graphene Properties, Synthesis and Applications: A Review. *JOM* **2023**, *75*, 614–630.

[6] Schwierz, F. Graphene transistors: status, prospects, and problems. *Proceedings of the IEEE* **2013**, *101*, 1567–1584.

[7] Ferreira, F. V.; Cividanes, L. D. S.; Brito, F. S.; Menezes, B. R. C. d.; Franceschi, W.; Nunes Simonetti, E. A.; Thim, G. P.; Ferreira, F. V.; Cividanes, L. D. S.; Brito, F. S. Functionalization of graphene and applications. *Functionalizing Graphene and Carbon Nanotubes: A Review* **2016**, 1–29.

[8] Solís-Fernández, P.; Bissett, M.; Ago, H. Synthesis, structure and applications of graphene-based 2D heterostructures. *Chemical Society Reviews* **2017**, *46*, 4572–4613.

[9] Ni, B.; Zhang, T.; Li, J.; Li, X.; Gao, H. Topological design of graphene. *Handbook of Graphene* **2019**, *2*, 1–44.

[10] Sholl, D. S.; Steckel, J. A. *Density functional theory: a practical introduction*; John Wiley & Sons, 2009.

[11] Giustino, F. *Materials modelling using density functional theory: properties and predictions*; Oxford University Press, 2014.

[12] Andreoni, W.; Yip, S. *Handbook of Materials Modeling: Applications: Current and Emerging Materials*; Springer, 2020.

[13] Martin, R. M. *Electronic structure: basic theory and practical methods*; Cambridge university press, 2004.

[14] Blinder, S. M.; House, J. E. *Mathematical physics in theoretical chemistry*; Elsevier, 2018.

[15] Kaxiras, E.; Joannopoulos, J. D. *Quantum theory of materials*; Cambridge university press, 2019.

[16] Koch, W.; Holthausen, M. C. *A chemist's guide to density functional theory*; John Wiley & Sons, 2015.

[17] Jensen, F. *Introduction to computational chemistry*; John wiley & sons, 2017.

[18] Hohenberg, P.; Kohn, W. Inhomogeneous electron gas. *Physical review* **1964**, *136*, B864.

[19] Parr, R. G. *Horizons of quantum chemistry*; Oxford, 1989; pp 5–15.

[20] Kohn, W.; Sham, L. J. Self-consistent equations including exchange and correlation effects. *Physical review* **1965**, *140*, A1133.

[21] Perdew, J. P.; Schmidt, K. Jacob's ladder of density functional approximations for the exchange-correlation energy. 2001.

[22] Hafner, J. Ab-initio simulations of materials using VASP: Density-functional theory and beyond. *Journal of computational chemistry* **2008**, *29*, 2044–2078.

[23] Furness, J. W.; Kaplan, A. D.; Ning, J.; Perdew, J. P.; Sun, J. Accurate and numerically efficient r2SCAN meta-generalized gradient approximation. *The journal of physical chemistry letters* **2020**, *11*, 8208–8215.

[24] Bartók, A. P.; Yates, J. R. Regularized SCAN functional. *The Journal of chemical physics* **2019**, *150*, 161101.

[25] Sun, J.; Ruzsinszky, A.; Perdew, J. P. Strongly constrained and appropriately normed semilocal density functional. *Physical review letters* **2015**, *115*, 036402.

[26] Kingsbury, R.; Gupta, A. S.; Bartel, C. J.; Munro, J. M.; Dwaraknath, S.; Horton, M.; Persson, K. A. Performance comparison of r 2 SCAN and SCAN metaGGA density functionals for solid materials via an automated, high-throughput computational workflow. *Physical Review Materials* **2022**, *6*, 013801.

[27] Peng, H.; Yang, Z.-H.; Sun, J.; Perdew, J. P. SCAN+ rVV10: A promising van der Waals density functional. *arXiv preprint arXiv:1510.05712* **2015**,

[28] Kothakonda, M.; Kaplan, A. D.; Isaacs, E. B.; Bartel, C. J.; Furness, J. W.; Ning, J.; Wolverton, C.; Perdew, J. P.; Sun, J. Testing the r2SCAN Density Functional for the Thermodynamic Stability of Solids with and without a van der Waals Correction. *ACS Materials Au* **2022**, *3*, 102–111.

[29] Kresse, G.; Furthmüller, J. Efficiency of ab-initio total energy calculations for metals and semiconductors using a plane-wave basis set. *Computational Materials Science* **1996**, *6*, 15 – 50.

[30] Kresse, G.; Hafner, J. Norm-conserving and ultrasoft pseudopotentials for first-row and transition elements. *Journal of Physics: Condensed Matter* **1994**, *6*, 8245.

[31] Bloch, F. Quantum mechanics of electrons in crystal lattices. *Z. Phys* **1928**, *52*, 555–600.

[32] Monkhorst, H. J.; Pack, J. D. Special points for Brillouin-zone integrations. *Phys. Rev. B* **1976**, *13*, 5188–5192.

[33] Pack, J. D.; Monkhorst, H. J. "Special points for Brillouin-zone integrations"—a reply. *Phys. Rev. B* **1977**, *16*, 1748–1749.

[34] Blöchl, P. E. Projector augmented-wave method. *Physical review B* **1994**, *50*, 17953.

[35] Kresse, G.; Joubert, D. From ultrasoft pseudopotentials to the projector augmented-wave method. *Physical review b* **1999**, *59*, 1758.

[36] Andrew, R. C.; Mapasha, R. E.; Ukpong, A. M.; Chetty, N. Mechanical properties of graphene and boronitrene. *Physical review B* **2012**, *85*, 125428.

[37] Bai, C. *Scanning tunneling microscopy and its application*; Springer Science & Business Media, 2000; Vol. 32.

[38] Tersoff, J.; Hamann, D. R. Theory of the scanning tunneling microscope. *Phys. Rev. B* **1985**, *31*, 805–813.

[39] https://www.vasp.at/wiki/index.php/POSCAR.

[40] https://www.vasp.at/wiki/index.php/POTCAR.

[41] https://www.vasp.at/wiki/index.php/INCAR.

[42] https://www.vasp.at/wiki/index.php/KPOINTS.

[43] https://www.vasp.at/wiki/index.php/CONTCAR.

[44] https://www.vasp.at/wiki/index.php/OUTCAR.

[45] https://www.vasp.at/wiki/index.php/OSZICAR.

[46] https://www.vasp.at/wiki/index.php/DOSCAR.

[47] https://www.vasp.at/wiki/index.php/PROCAR.

[48] Hofer, W. A Guide to simulation of STM images and spectra from first principles: bSKAN 3.6. *Surface Science Research Centre, The University of Liverpool, Liverpool, UK* **2005**, 60.

[49] Nakada, K.; Ishii, A. DFT calculation for adatom adsorption on graphene. *Graphene Simulation* **2011**, 1–19.

[50] Allen, M. J.; Tung, V. C.; Kaner, R. B. Honeycomb carbon: a review of graphene. *Chemical reviews* **2010**, *110*, 132–145.

[51] Garzon, D. Electronic structure of nobel-graphene based superlattices. 2021; Available at `https://repositorio.yachaytech.edu.ec/handle/123456789/449`.

[52] Balog, R.; Jørgensen, B.; Nilsson, L.; Andersen, M.; Rienks, E.; Bianchi, M.; Fanetti, M.; Lægsgaard, E.; Baraldi, A.; Lizzit, S. Bandgap opening in graphene induced by patterned hydrogen adsorption. *Nature materials* **2010**, *9*, 315–319.

[53] Lehtinen, P. O.; Krasheninnikov, A. V.; Foster, A. S.; Nieminen, R. M. The magnetic nature of intrinsic and irradiation-induced defects in carbon systems. *Carbonbased magnetism. An overview of the magnetism of metal free carbon-based compounds and materials* **2006**, 371–396.